

Cryomagma ascent on Europa

Elodie Lesage¹, H       Massol¹, Fr       Schmidt¹

¹ GEOPS, Univ. Paris-Sud, CNRS, Universit   Paris-Saclay, Rue du Belv      , B   . 504-509, 91405 Orsay, France

Abstract

Europa’s surface exhibits morphological features which, associated with a low crater density, might be interpreted to have formed as a result of recent cryovolcanic activity. In particular, the morphology of smooth deposits covering parts of the surface, and their relationship to the surrounding terrains, suggest that they result from liquid extrusions. Furthermore, recent literature suggests that the emplacement of liquid-related features, such as double ridges, lenticulae and chaos could result from the presence of liquid reservoirs beneath the surface. We model the ascent of liquid water through a fracture or a pipe-like conduit from a subsurface reservoir to Europa’s surface and calculate the eruption time-scale and the total volume extruded during the eruption, as a function of the reservoir volume and depth. We also estimate the freezing time of a subsurface reservoir necessary to trigger an eruption. Our model is derived for pure liquid water and for a briny mixture outlined by Kargel (1991): 81 wt% H₂O + 16 wt% MgSO₄ + 3 wt% Na₂SO₄. Considering compositional data for salt impurities for Europa, we discuss the effect of MgSO₄ and Na₂SO₄ on the cryomagma freezing time-scale and ascent. For plausible reservoir volumes and depths in the range of $10^6 \text{ m}^3 \leq V \leq 10^{10} \text{ m}^3$ and $1 \text{ km} \leq H \leq 10 \text{ km}$ respectively, the total extruded cryolava volume ranges from 10^3 m^3 to 10^8 m^3 and the duration of the eruptions varies from few minutes to few tens of hours. The freezing time-scale of the cryomagma reservoirs varies with cryomagma composition and the temperature gradient in the ice shell: from a few days to a thousand years for pure water cryomagma, and from a few months to a 10^4 years for briny cryomagma.

Keywords: cryovolcanism, icy satellite, reservoir, freezing, salt inclusion

1. Introduction

Spectroscopic analysis of Europa shows a surface entirely covered with water ice mixed with impurities such as salts and sulfates (Dalton, 2007; Ligier et al., 2016), having a very young age of approximately 70 My (Zahnle et al., 2003), thus implying active resurfacing processes. Data from the Galileo spacecraft acquired

between 1995 and 2001 provided several clues indicating the presence of an internal global ocean beneath the ice shell. First of all, Europa possesses an induced magnetic field, consistent with the presence of a liquid salty water layer (Khurana et al., 1998). Also, the orientation of some large scale linear features seems to have changed over time, implying the rotation of the ice shell, which could not be possible without a very low viscosity layer between the mantle and the surface (Pappalardo et al., 1999; Schenk et al., 2008). The measurement of the Europa's moment of inertia shows that the total water and ice layer is 80 to 170 km thick (Anderson, 1998; Vance et al., 2018). The thickness of the ice layer cannot be inferred from the moment of inertia, but it is deduced from numerical modeling of Europa's tidal dissipation (Tobie et al., 2003; Quick and Marsh, 2015), the maximum expected ice crust thickness being 30 km. Thermal profiles modeled for Europa's ice shell suggests an outer 10 km thick conductive layer (Tobie et al., 2003) expected to behave as an elastic material (Nimmo, 2004a) above an approximately 10 to 20 km thick convective layer (Tobie et al., 2003; Quick and Marsh, 2015).

The presence of an internal global liquid water ocean is even more interesting as it is supposed to be in contact with the silicate mantle. In fact, the moderate thickness of the internal ocean does not allow the presence of high pressure ice phases at the bottom of the ocean (Anderson, 1998). The possibility of a rich chemical exchange between the rocky mantle and the ocean (Kargel, 1991) makes Europa a candidate to support the development of life forms (Greenberg and Geissler, 2002). Two missions in development, JUICE (ESA) and Europa Clipper (NASA), aim to study the surface and subsurface of the satellite. If biosignatures are produced deep in Europa's ocean, they need to be brought at the surface to potentially be detected by these spacecrafts. In this context, understanding whether, where, and for how long liquid water is erupted at the surface should help to inform the missions as to where biosignatures are most likely to be found.

The images of the surface acquired during the Galileo mission show a great diversity of geological features on Europa indicating active internal processes (Greenberg and Geissler, 2002; Fagents, 2003; Kattenhorn and Prockter, 2014). Among those features, smooth deposits and lobate features cover parts of the surface (see Fig. 1). As suggested by their morphologies and relationship to the surrounding terrains, it seems possible that these features may result from liquid extrusions at the surface (Miyamoto et al., 2005). Manga and Wang (2007) showed that liquid water is unlikely to rise directly from the internal ocean to the surface through large fractures because of the extremely high pressure required for this mechanism to work. For example, even for an extreme thickness of 50 km of ice, freezing of a few kilometers of water in the ocean would induce a 1-10 kPa overpressure, which is enough to propagate a fracture over the ice crust thickness (Manga and Wang,

2007; Neveu et al., 2015) but not to bring water from the ocean to the surface: a few MPa are necessary to drive the water past the level of neutral buoyancy. On the other hand, recent literature demonstrated the possibility of the emplacement of common geological features at Europa’s surface, such as double ridges (Dombard et al., 2013; Johnston and Montési, 2014; Dameron and Burr, 2018), chaos (Greenberg et al., 1999; Schmidt et al., 2011) and lenticulae (Manga and Michaut, 2017) by the presence of near-surface liquid water reservoirs. Although Craft et al. (2016) found emplacement of horizontal water sills to be challenging through hydrofracturing mechanisms, the morphological studies of the features cited above remain in good agreement with models taking into account warm water lenses at shallow depths.

In this study, we focus on effusive water flows possibly generated by cryovolcanic activity, i.e. implying storage and eruption of liquid. We consider the cryomagma as a very low viscosity fluid, composed of pure or briny water. We follow the eruption mechanism proposed by Fagents (2003): liquid water, stored in a reservoir within Europa’s ice shell, cools and freezes over time, generating an overpressure within the reservoir that eventually leads to fracturing of the surrounding ice. Fagents (2003) demonstrated the feasibility of bringing water at the surface from a freezing reservoir, and presented the range of pressures and depths for which liquid water could reach the surface. However, that study did not take into account water transport dynamics and time-scales. Recently, Quick and Marsh (2016) calculated the ascent velocity necessary for the cryomagma to reach the surface without freezing in the conduit. They found, for example, a minimum velocity of $\sim 2.5 \times 10^{-2} \text{ m s}^{-1}$ for a 4 m wide and 10 km long fracture. Similarly, Craft et al. (2016) found, for a turbulent pure water flow through a 8 km tall, 10-100 m wide fracture, a flow velocity faster than the freezing time. Hence, the feasibility of bringing liquid water to the surface has been demonstrated and is used in our model.

Following the previous work, this study aims to estimate the order of magnitude of the eruption time-scale and fluid volume erupted at the surface during an effusive cryovolcanic event. We consider, as initial conditions, a reservoir as a spherical cavity at some depth in the ice shell, filled with pure or briny liquid water at lithostatic pressure. The cryomagma freezes over time and generates an overpressure in the reservoir that fractures its wall when the tensile stress exceeds the tensile strength of the ice. The time required to reach this critical pressure gives the time-scale required to generate an eruption. The cryomagma is then driven to the surface through a fracture, and we calculate the flow velocity and the time evolution of the reservoir pressure during the eruption, as well as the eruption duration and the volume of cryolava erupted at the surface at the end of the eruption.

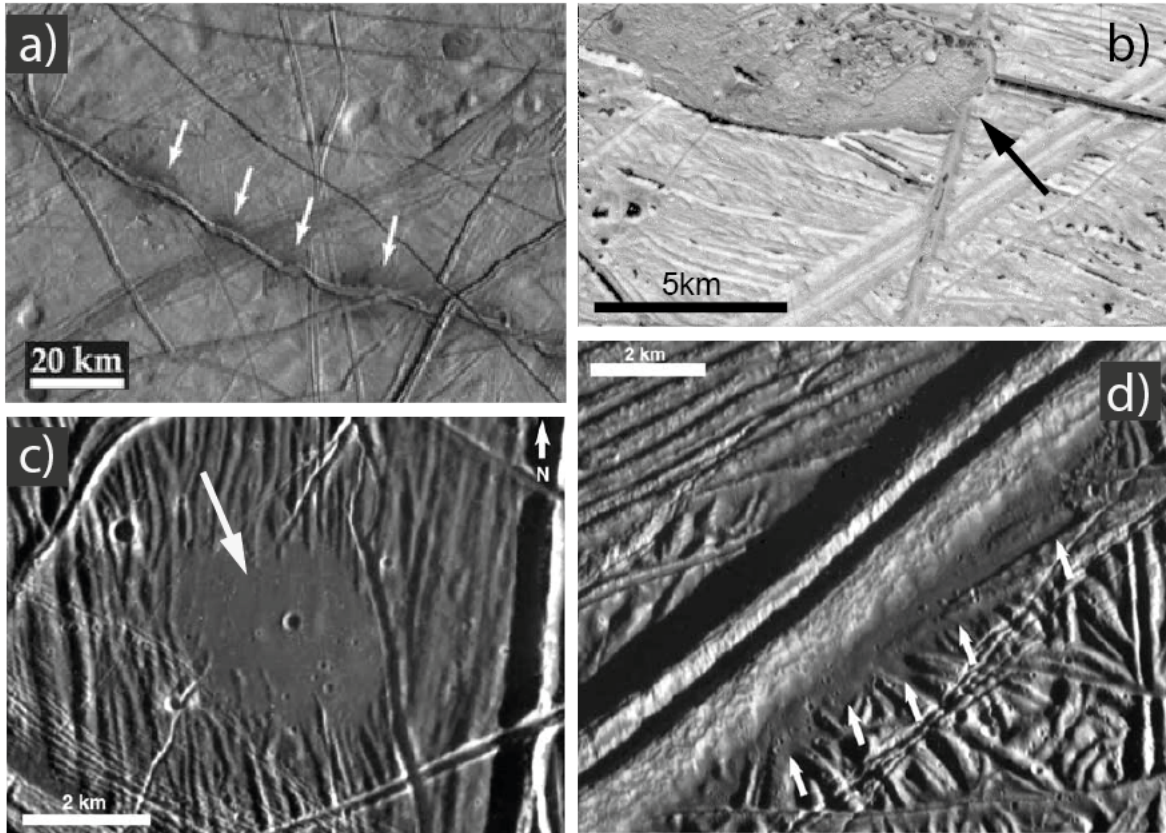


Figure 1: Example of European surface features that might have cryovolcanic origins. a) Low albedo zones along a double ridge (Quick and Marsh, 2016) (Image ID: 15E0003); b) Chaos-like feature with a lobate structure (Image ID: 15E0071); c) Circular smooth deposit (Fagents, 2003) (6°N, 327° W); d) Smooth deposit flanking a double ridge (Fagents, 2003) (Image ID: E6E0073).

2. Model

2.1. Model assumptions

Various processes could explain the formation of cryomagmatic reservoirs in the ice shell. For instance, Kalousová et al. (2016) showed that the heat generated by tidally activated faults might be sufficient to produce water lenses in the ice crust. Mitri and Showman (2008) showed that partial melting of the bulk ice is also possible due to the tidal heating itself, a process that might be especially effective in warm convective plumes due to the temperature dependence of the tidal dissipation rate. Compositional heterogeneities in the ice could also generate local temperature maxima and may lead to local melting (Prieto-Ballesteros and Kargel, 2005; Quick and Marsh, 2015).

Since there are no available geophysical measurements of characterizing reservoir geometries within Europa’s surface, we assume a spherical liquid-filled reservoir surrounded by ice. The reservoir is filled with pure or briny liquid water, called hereafter “cryomagma”, at isostatic pressure P_0 . Moreover, we limit our model to the upper 10 kilometers of the ice shell, which are expected to behave as a conductive elastic material due to the very low temperatures (Tobie et al., 2003). The assumption of elastic behavior of the ice can be verified by the Maxwell time $\tau_M = \mu_{ice}/E$ where μ_{ice} is the ice viscosity and E the Young’s modulus of ice, which gives the time-scale under which a material responds elastically. With $\mu_{ice} = 10^{33}$ Pa s (Hillier and Squyres, 1991), and $E \simeq 9$ GPa (Gammon et al., 1983; Petrenko and Whitworth, 2002), the Maxwell time of conductive ice should be at least a few million years near the surface, and the ice is likely to behave as an elastic material for the process explored in our study and under certain conditions. However, for higher temperatures, the Maxwell relaxation time of water ice is lower, which means that the ice surrounding the reservoir could react in a viscous manner if the volume of the reservoir increases in a time greater than the Maxwell time. The viscous behavior of the ice is not taken into account here, and our model is limited to ice temperatures for which the surrounding reservoir ice behaves elastically. This limitation is investigated further in section 4.

A correct estimation of the duration of an eruptive event and the erupted volume requires modeling of two distinct processes: (1) the freezing and pressurization of the cryomagma reservoir until it reaches the necessary overpressure in order to erupt (see section 2.2 and Fig. 2(a) and (b)), and (2) the cryomagma ascent to the satellite’s surface after the fracture opens (see section 2.3 and Fig. 2(c)). In this paper, we consider two cryomagma compositions: (1) pure water and (2) a briny cryomagma, the composition of which

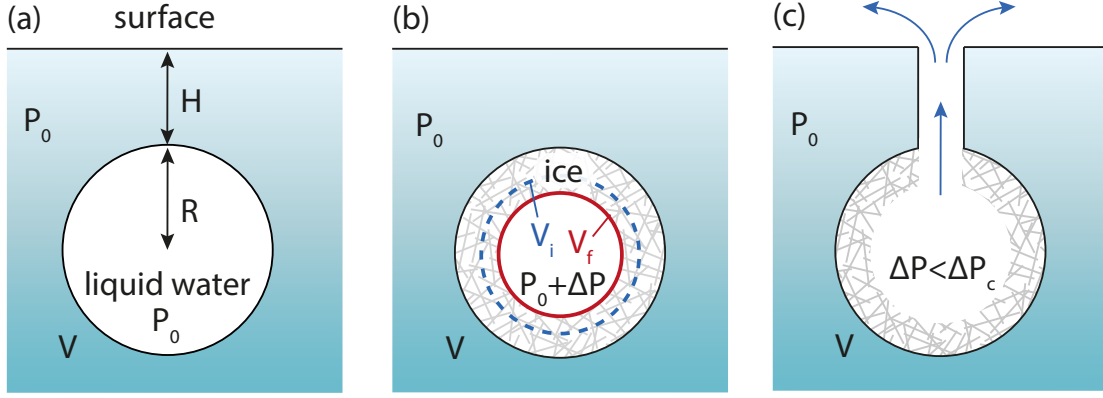


Figure 2: Schematic representation of a cryomagma reservoir of volume V and radius R , located at depth H under the surface. Liquid cryomagma is represented in white whereas frozen cryomagma is hatched in grey. (a) The reservoir is filled with pure or briny liquid water at isostatic pressure P_0 . (b) An initial liquid volume V_i freezes and becomes a volume V_f of ice, inducing an overpressure ΔP in the reservoir (see section 2.2). (c) When the pressure reaches a critical value ΔP_c , the wall fractures and the pressurized liquid rises to the surface through a H long fracture (see section 2.3).

is detailed below.

Europa's global internal ocean is probably salty as indicated by the Galileo flybys (Khurana et al., 1998), but its precise composition remains unknown. After Kargel (1991) and based on carbonaceous chondrite composition and chemical evolution in aqueous environment, two main impurities are expected to be present in the Europa's aqueous crust: magnesium sulfate, MgSO_4 , which represents 75% of carbonaceous chondrite mass (Hogenboom et al., 1995), and sodium sulfate, Na_2SO_4 , the second most abundant chondritic component (Kargel, 1991; Hogenboom et al., 1995; Dalton, 2007). Other minor components are expected to be present in Europa's crust and ocean (Kargel 1991; Hogenboom et al. 1995; Neveu et al. 2015; see Quick and Marsh, 2016 for a review), which is confirmed by spectroscopic studies (e.g. Dalton, 2007; Ligier et al., 2016): chlorides such as MgCl_2 , NaCl , CaCl_2 and KCl , and sulfates of K, Mn, Ca and Ni.

Existing literature uses various brine compositions for Europa, and we summarize these in Table 1 and give the main physical/chemical properties of the hydrates likely to be found on Europa (solid/liquid densities, melting/eutectic temperatures, and viscosities at the eutectic temperatures). In this study we assume the composition outlined by Kargel (1991): 81 wt% H_2O + 16 wt% MgSO_4 + 3 wt% Na_2SO_4 . We use this liquid composition as a reference for briny cryomagma in our calculations (in bold in Table 1). Concerning the minor components, they are expected to represent ~ 1 wt% of Europa's ice shell composition (Kargel, 1991), and therefore they should not have a strong influence on the water and ice densities. Nevertheless, their physical properties are also summarized in Table 1.

Our simulations do not take into account the case of a liquid having a lower density than the corresponding solid phase, i.e. $\rho_i > \rho_w$. This might be the case if ammonia were present in the cryomagma, but this seems unlikely on Europa (Kargel, 1991; Dalton, 2007). In that case, freezing alone could not cause an excess pressure in the reservoir. However, the liquid cryomagma would be buoyant in the ice shell, and ascent in an open fracture would be promoted.

To model a cryovolcanic reservoir, we use the same approach as Fagents (2003), summarized in Fig. 2: the fluid contained in a reservoir cools over time, and eventually freezes. Section 2.2.3 details this process and how we calculate the necessary time to fracture the reservoir wall. The reservoir overpressure ΔP induced by freezing generates a tensile stress on the reservoir wall and when this stress overcomes the tensile strength of the ice, the wall fractures in Mode 1 (opening) type of fracturing. Once a fracture is opened, the fluid can flow toward the surface. The eruption is driven by the pressure gradient between the reservoir and the satellite's surface. The eruption ends when the overpressure is balanced by the weight of the cryomagma column in the fracture (see section 2.3.2). All notation used in this section are summarized in Table 2.

Table 2: Table of variables used in this study.

Symbol	Definition	Value	Unit	Reference
a	fracture major semi-axis	100 (except when specified as varying)	m	
A	fracture/pipe-like conduit cross sectional area		m ²	
b	fracture minor semi-axis	1 (except when specified as varying)	m	
c_p	pure water ice heat capacity	2×10^3	J kg ⁻¹ K ⁻¹	Hobbs, 1975
D_h	fracture/pipe-like conduit hydraulic diameter	Eq. (22)	m	Bejan, 1993
E	Young's Modulus of the ice	$\simeq 9 \times 10^9$	Pa	Nimmo, 2004b
f	Fanning friction factor in the conduit	0.01	-	Bird et al., 1960 (First Edition)

g	gravity on Europa	1.315	m s^{-2}	Robert T. Pappalardo, 2009
H	depth to the top of the reservoir	1 to 10 km	m	
k_l	liquid water thermal conductivity	0.6	$\text{W m}^{-1} \text{K}^{-1}$	Blumm and Lindemann, 2003
k_s	water ice thermal conductivity	2.3 at 273 K	$\text{W m}^{-1} \text{K}^{-1}$	Hobbs, 1975
K	bulk modulus of the ice	8.6×10^9	Pa	
K_c	ice fracture toughness	0.05 to 0.2	$\text{MPa m}^{1/2}$	Litwin et al., 2012
K_t	crack-tip stress intensity factor	Eq. (19)	Pa m^{-2}	Lister and Kerr, 1991 and Rubin, 1993
L_s	latent heat of solidification of pure water	3×10^5	$\text{J K}^{-1} \text{kg}^{-1}$	Hobbs, 1975
n	fraction of liquid that freezes		-	
n_c	critical fraction of liquid that freezes	Eq. (13)	-	
p	fracture/conduit perimeter		m	
P_0	lithostatic pressure		Pa	
P_c	critical pressure in the reservoir		Pa	
P_{open}	pressure necessary to keep a fracture open	Eq. (20)	Pa	Sigurdsson et al., 1999
P_{tot}	total pressure in the reservoir		Pa	
ΔP	overpressure generated by freezing		Pa	
ΔP_c	critical overpressure	Eq. (12)	Pa	
q	heat lost by convection	Eq. (15)	W m^{-2}	
R	reservoir radius	50 to 1300	m	
Ra	Rayleigh number	Eq. (14)	-	
$S(t)$	location of the solidification front in the reservoir		m	

S_c	location of the critical solidification front	Eq. (18)	m	
t	time		s	
dt	time step used in numerical modelling		s	
$T_0(z, t)$	reservoir frozen part temperature		K	
$T_1(z, t)$	temperature outside the reservoir		K	
T_{cold}	ice temperature at depth H far from the reservoir		K	
T_m	pure water melting temperature	273	K	Rumble, 2002
U	liquid mean velocity in the fracture during the eruption	Eq. (25)	m s^{-1}	
V	total volume of the reservoir	10^6 to 10^{10}	m^3	
V_e	volume of liquid emitted at the surface		m^3	
V_f	actual volume of liquid after freezing	Eq. (4)	m^3	
V_i	virtual volume of the liquid if not compressed	Eq. (3)	m^3	
ΔT	difference between the liquid temperature and melting temperature	$T_l - T_m$	K	
α	liquid water thermal expansion coefficient	10^{-3}	K^{-1}	Craft et al., 2016
κ_l	liquid water thermal diffusivity	10^{-7}	$\text{m}^2 \text{s}^{-1}$	
κ_s	water ice thermal diffusivity	$\kappa_s = \frac{k_s}{\rho c_p}$	$\text{m}^2 \text{s}^{-1}$	
λ	constant related to heat transfer	$\lambda = \frac{S}{2\sqrt{\kappa_s t}}$	-	
μ	liquid water dynamic viscosity	10^{-3}	Pa s	
μ_{ice}	ice dynamic viscosity	Eq. (26)	Pa s	Hillier and Squyres, 1991
ν	Poisson's ratio of ice	$\simeq 0.325$	-	Litwin et al., 2012
ρ_l	liquid density	1000 for pure water 1180 for briny water	kg m^{-3}	Rumble, 2002 and Kargel, 1991

ρ_s	ice density	900 for pure water ice 1130 for briny water ice	kg m^{-3}	Rumble, 2002 and Kargel, 1991
ρ_{li}	virtual density of the liquid if not compressed		kg m^{-3}	
ρ_{lf}	actual density of liquid after partial reservoir volume freezing	Eq. (6)	kg m^{-3}	
σ_0	lithostatic pressure around the reservoir	$\sigma_0 = \rho_i g H$	Pa	
σ_c	pure water ice tensile strength	1.7×10^6 at 100 K, 1×10^6 at 200 K, 0.5×10^6 at 250 K	Pa	Litwin et al., 2012
$\sigma_{\theta\theta}$	tensile strength of the reservoir wall	Eq. (9)	Pa	Sammis and Julian, 1987 and McLeod and Tait, 1999
τ_M	Maxwell relaxation time of the ice time required to cool the reservoir	μ_{ice}/E	s	
$\tau_{cooling}$	from initial temperature T_l to freezing point T_m	Eq. (16)	s	
τ_c	solidification time-scale of the reservoir	Eq. (17)	s	
$\tau_{eruption}$	total duration of the eruption		s	
τ_w	shear stress on the fracture/pipe-like conduit walls	$\tau_w = \frac{1}{2} f \rho_l U^2$	Pa	Bird et al., 1960 (First Edition)
χ	pure liquid water compressibility	5×10^{-10}	Pa^{-1}	Fine and Millero, 1973

2.2. Cryomagma freezing

2.2.1. Overpressure in a cooling cryomagmatic reservoir

As the initial condition, we assume that the total volume of the reservoir V is filled with pure or briny liquid water. The reservoir would cool with time, and we want to estimate the overpressure ΔP generated when a volume fraction of liquid n ($n = 1 - V_i/V$) freezes, with V_i being the initial volume occupied by the fraction of liquid remaining in a liquid state after freezing (see Fig. 2b). After freezing, the remaining liquid

Table 1: Properties of candidate impurities in Europa’s ocean and ice. The predicted composition (after Kargel 1991) in bold is used in our calculations. Specific heat capacities are given for eutectic temperatures.

Solution	Liquid density (kg m^{-3})	Solid density (kg m^{-3})	Eutectic liquid	Melting temperature (K)	Eutectic temperature (K)	Specific heat capacity c_p ($\text{J g}^{-1} \text{K}^{-1}$)
Major hydrates						
Water (ice I)	1000	917	2×10^{-3}	273	-	
$\text{MgSO}_4\text{-}7\text{H}_2\text{O}$ (19.6 wt% MgSO_4)	1226	1670		321.6	268	1.44
$\text{MgSO}_4\text{-}11\text{H}_2\text{O}$ (17 wt% MgSO_4)	1180	1510		275	269	
$\text{Na}_2\text{SO}_4\text{-}10\text{H}_2\text{O}$ (4 wt% Na_2SO_4)	1038	1460		305.6	272	1.825
Minor hydrates						
$\text{KCl-nH}_2\text{O}$ (19.9 wt% KCl)	1132				262	
$\text{NaCl-}2\text{H}_2\text{O}$ (23 wt% NaCl)	1200	1610	5×10^{-3}	273.3	252.4	
$\text{MgCl}_2\text{-nH}_2\text{O}$ (21 wt% MgCl_2)	1200		2×10^{-2}		239.4	
$\text{CaCl}_2\text{-}6\text{H}_2\text{O}$ (30 wt% CaCl_2)	1282		4×10^{-2}		223.2	
$\text{H}_2\text{SO}_4\text{-}6.5\text{H}_2\text{O}$ (35.7 wt% H_2SO_4)	1283	1540		219.4	211.3	
$\text{H}_2\text{SO}_4\text{-}4\text{H}_2\text{O}$ (37 wt% H_2SO_4)	1290				198	
Mixtures						
47 wt% H_2O + 53 wt% $\text{MgSO}_4\text{-}12\text{H}_2\text{O}$	1180	1126	6×10^{-3}			
81 wt% H_2O + 16 wt% MgSO_4 + 3 wt% Na_2SO_4	1180 to 1190	1133	1×10^{-2}		268	
Data from Kargel, 1991; Hogenboom et al., 1995; Rumble, 2002; Prieto-Ballesteros and Kargel, 2005; McCarthy et al., 2007; Quick and Marsh, 2016.						

occupies a volume V_f with $V_f < V_i$, corresponding to the pressure increase ΔP from the compression of the liquid (see Fig. 2b). This overpressure depends on the liquid water compressibility χ :

$$\chi = -\frac{1}{V} \frac{\partial V}{\partial P} \quad (1)$$

where V is the liquid volume and P the liquid pressure. Here, we consider a constant compressibility for pure water. A value of $\chi = 5 \times 10^{-10} \text{ Pa}^{-1}$ is in agreement with the work of Fine and Millero (1973) for pressure of order of a few to 10 MPa. As a comparison, sea water under the same pressure and near-zero temperature has a compressibility of $\simeq 4.5 \times 10^{-10} \text{ Pa}^{-1}$ (Safarov et al., 2009), so the addition of salts is not expected to change significantly our results. ΔP then follows the Eq. (1) in our case as:

$$\Delta P = -\frac{1}{\chi} \ln \left(\frac{V_f}{V_i} \right) \quad (2)$$

Keeping in mind that mass is conserved during freezing, V_i and V_f are defined as:

$$V_i(n) = (1 - n) V \quad (3)$$

$$V_f(n) = \left(1 - n \frac{\rho_l}{\rho_s} \right) V \quad (4)$$

where ρ_l is the liquid density and ρ_s is the ice density.

Combining Eq. (2), (3) and (4), we obtain the fraction of cryomagma n that has to freeze in order to induce the overpressure ΔP :

$$n = \frac{\exp(\chi \Delta P) - 1}{\frac{\rho_l}{\rho_s} \exp(\chi \Delta P) - 1} \quad (5)$$

Note that the density ρ_{lf} of the liquid contained in the reservoir after freezing is given by:

$$\rho_{lf} = \rho_{li} \frac{V_i(n)}{V_f(n)} \quad (6)$$

where ρ_{li} is the liquid density before being compressed.

We further assume that the reservoir wall is static and undeformable by elastic load. We discuss this assumption in section 3.1.

2.2.2. Tensile failure of a cooling cryomagmatic reservoir

In this model, we assume that the ice reservoir wall will fracture in a tensile Mode I (opening) manner, similar to that of magma chambers on Earth (McLeod and Tait, 1999). The maximum pressure that could be achieved in the reservoir is then dictated by the tensile strength of the ice (Rubin, 1993; McLeod and Tait, 1999). Litwin et al. (2012) measured this tensile strength for different temperatures and grain sizes of polycrystalline ice. Their measurements were made in a cold medium at temperatures down to 120 K, which are appropriate for planetary bodies, and in particular the icy satellites. It is expected that ice porosity has an influence on the tensile strength of the ice shell in that a higher porosity (possibly due to previous weakening of the ice crust) could lower the tensile strength of the ice crust. It has been suggested that failure of Europa’s ice shell might be favored due to weakening from cyclic tidal forcing and heating (Greenberg and Geissler, 2002; Lee et al., 2005; Harada and Kurita, 2006; Quillen et al., 2016), and also due to global cooling stress (Nimmo, 2004a; Manga and Wang, 2007). Nevertheless, we only know the ice structure of the first millimeter of the surface of Europa (Hansen, 2004), so we use the ice tensile strength value σ_c measured by Litwin et al. (2012) for pure water ice of a few millimeters mean grain size. We infer a temperature gradient within the ice shell in agreement with the work of Quick and Marsh (2015): at a depth of 10 km in the ice shell, the temperature is at least 200 K, which gives $\sigma_{c,200K} = 1$ MPa (see Litwin et al. (2012)), and at the surface, the temperature is approximately 100 K. The measurements of Litwin et al. (2012) are made at temperatures above 120 K, but their results follow a linear trend, so we extrapolated a mean value $\sigma_{c,100K} = 1.7$ MPa from their data. This temperature gradient is taken as a reference gradient and represents the coldest possible case for a 30 km ice shell (Quick and Marsh, 2015). As the temperature gradient could be quite variable, depending on the ice shell thickness, local heating by thermal plumes, and tidal heating (Tobie et al., 2003; Mitri and Showman, 2008; Quick and Marsh, 2015), the impact of the thermal structure on the results is discussed in section 3.3. We also make the assumption of a conductive lid extending from the surface to a depth of 10 km with a linear temperature variation in the ice shell from 0 to 10 km. As in Litwin et al. (2012), we consider the linear dependance of tensile strength on temperature:

$$\sigma_c = \sigma_{c,100K} + \frac{(\sigma_{c,200K} - \sigma_{c,100K})}{10^4} H \quad (7)$$

where H is the top of the reservoir depth. As the minimum stress is at the top of the reservoir, we consider the case of a vertical fracture starting from this point. The lithostatic pressure induces a stress field

$\sigma^0 = \rho_s g H$ where ρ_s is the ice density. The reservoir is filled with liquid which generates an overpressure ΔP as it freezes. Thus, the total pressure in the reservoir is given by:

$$P_{tot} = \rho_s g H + \Delta P \quad (8)$$

where g is the gravity on Europa.

The overpressure ΔP generates a tensile stress $\sigma_{\theta\theta}$ on the reservoir wall, which is given by (Sammis and Julian, 1987; McLeod and Tait, 1999):

$$\sigma_{\theta\theta} = \sigma^0 \left[1 + \frac{1}{2} \left(1 - \frac{P_{tot}}{\sigma^0} \right) \right] \quad (9)$$

where $\sigma^0 = \rho_s g H$ is the lithostatic pressure field far from the reservoir. If $\sigma_{\theta\theta}$ exceeds a critical value σ_c , the reservoir wall fractures. We consider compressive stresses as positive values, so tensile failure occurs if:

$$\sigma_{\theta\theta} \geq -\sigma_c \quad (10)$$

Combining Eq. (8), (9) and (10), we deduce that the wall fractures if the overpressure reaches a critical value ΔP_c :

$$\Delta P_c = 2 (\sigma_c + \sigma^0) \quad (11)$$

or:

$$\Delta P_c = 2 (\sigma_c + \rho_s g H) \quad (12)$$

Eq. (12) shows that the critical overpressure ΔP_c depends on the reservoir depth.

Using (5), the critical fraction of liquid n_c that has to freeze to generate the critical overpressure ΔP_c is given by:

$$n_c = \frac{\exp(\chi \Delta P_c) - 1}{\frac{\rho_l}{\rho_s} \exp(\chi \Delta P_c) - 1} \quad (13)$$

2.2.3. Cooling and freezing time-scales

In this section we aim to estimate the time-scale required to cool a reservoir at initial temperature T_l and freeze a fraction n_c to trigger an eruption. The heat exchange between the fluid in the reservoir and the surrounding ice is the key to understanding this process. The heat exchange regime is described by the

Rayleigh number Ra (Bejan, 1993):

$$Ra = \frac{g\rho_l\alpha R^3\Delta T}{\mu\kappa_l} \quad (14)$$

with ρ_l the liquid density, α the thermal expansion coefficient, R the reservoir radius, $\Delta T = T_l - T_m$ the difference between the liquid temperature T_l and the melting temperature T_m (taken as $T_m = 273$ K here), μ the liquid dynamic viscosity and κ_l the liquid thermal diffusivity. Ra gives the cooling regime of the reservoir: $Ra < 10^3$ indicates a conductive cooling, whereas $Ra > 10^3$ means that the liquid is convective. We take the values $g = 1.315 \text{ m}^2 \text{ s}^{-2}$, $\rho_l \simeq 1000 \text{ kg m}^3$, $\alpha \simeq 10^{-3} \text{ K}^{-1}$, $\mu \simeq 10^{-3} \text{ Pa s}$, and $\kappa_l \simeq 10^{-7} \text{ m}^2 \text{ s}^{-1}$. As the liquid temperature is unlikely to be much greater than T_m , we calculate Ra for $\Delta T = 1$ K and $\Delta T = 10$ K. For reservoir radius varying from $\simeq 100$ m to $\simeq 1000$ m, we find $Ra \geq 10^{15}$ for $\Delta T = 1$ K and $Ra \geq 10^{16}$ for $\Delta T = 10$ K. These very high Ra indicate a vigorous convection in the reservoir. The reservoir heat loss by convection is estimated as (Craft et al., 2016):

$$q \sim \frac{k_l\Delta T}{R} Ra^{1/3} \quad (15)$$

where k_l stands for the liquid water thermal conductivity and is taken as $k_l \simeq 0.6 \text{ W m}^{-1} \text{ K}^{-1}$. We obtain $q \simeq 660 \text{ W m}^{-2}$ for $\Delta T = 1$ K and $q \simeq 1.5 \times 10^4 \text{ W m}^{-2}$ for $\Delta T = 10$ K. The time required to cool the reservoir from an initial temperature T_l to the melting temperature T_m is thus estimated as:

$$\tau_{cooling} \simeq \frac{\rho_l R c_p \Delta T}{q} \quad (16)$$

where $c_p \simeq 2 \times 10^3 \text{ J kg}^{-1} \text{ K}^{-1}$ is the liquid water specific heat capacity (Hobbs, 1975). Eq. (16) gives $\tau_{cooling} < 4$ days for the smallest reservoirs ($R \simeq 100$ m) and $\tau_{cooling} < 40$ days for the largest reservoirs considered here ($R \simeq 1000$ m), which means that the convection very efficiently removes heat from the reservoir. Once the reservoir reaches the melting temperature T_m , the liquid does not cool further, but will instead change phase.

At this point, the liquid remains at uniform temperature T_m until it freezes so there is no more temperature gradient to drive convection. In the case of a briny cryomagma, the liquid phase is expected to be enriched in salts during freezing, but in this study we neglect a potential density driven convection. Thus, we make the assumption that convection stops when the liquid is at temperature T_m and we model the cryomagma freezing due to heat conduction through the ice.

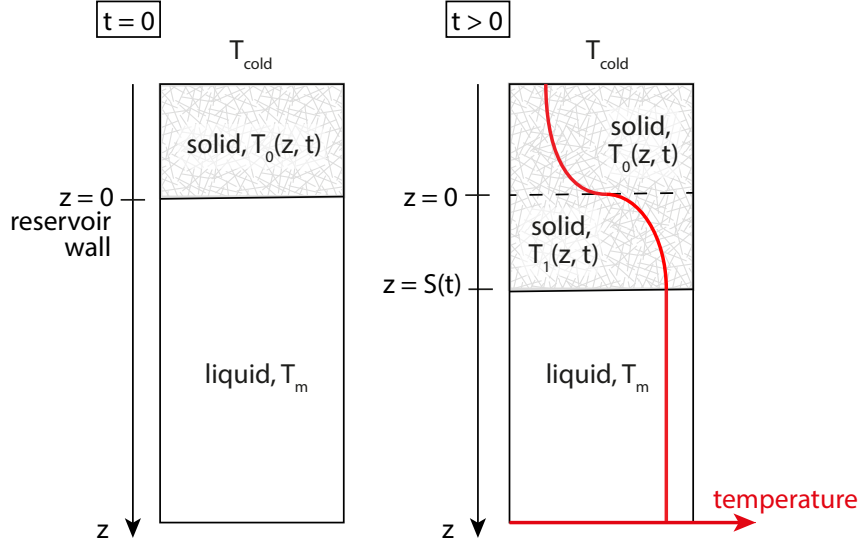


Figure 3: Summary of the Stefan problem. At time $t = 0$, the reservoir is totally filled with liquid cryomagma, at a uniform melting temperature T_m . Far from the reservoir (i.e. for $z \rightarrow -\infty$), the ice is at constant temperature T_{cold} . For $t > 0$, the liquid in the reservoir progressively freezes: the solidification front progresses in direction of the center of the reservoir. At time t , the solidification front is located at the position $S(t)$. The temperature profiles in regions $z > 0$ and $0 < z < S(t)$ are respectively named T_0 and T_1 , whereas the temperature of the liquid part of the reservoir remains constant at T_m .

In order to estimate the time required to freeze a fraction n_c of cryomagma by conduction, we solve the Stefan problem (see Appendix). The liquid in contact with the reservoir wall starts to freeze, and the solidification front progresses toward the center of the reservoir (see Fig. 3). The Stefan problem gives the position of the solidification front as a function of time. As we know the critical fraction of cryomagma n_c required to freeze to fracture the reservoir wall, we can infer a critical position of the solidification front, called S_c hereafter, and deduce the time τ_c required to reach it. Since the volume of the reservoir necessary to freeze is a thin ice shell layer covering the reservoir wall (less than 10% of the reservoir radius for a briny cryomagma and 5% for a pure one), we solve the Stefan problem in 1D using cartesian coordinates, which is valid to give an order of magnitude of the freezing time-scale. The freezing time-scale is then given by (see Appendix for details):

$$\tau_c = \left(\frac{S_c}{2\lambda\sqrt{\kappa_s}} \right)^2 \quad (17)$$

where S_c is the position of the solidification front corresponding to ΔP_c , i.e. the thickness of the cryomagma layer necessary to freeze in order to generate an eruption, κ_s is the ice thermal diffusivity, and λ is a constant

that is a solution of the thermal transfer equations. Diffusivity κ_s can be expressed as a function of the water ice thermal conductivity k_s , the pure water ice heat capacity c_p and the water ice density ρ_s : $\kappa_s = \frac{k_s}{\rho_s c_p}$. Prieto-Ballesteros and Kargel (2005) investigated the thermal conductivity and heat capacity of some salts relevant for Europa with various hydration states. However, the salt concentration might be quite variable in the ice shell due to local depletion or enrichment of impurities. Moreover, salts go preferentially in the liquid phase during freezing so the resulting bulk ice should be close to pure H₂O. For these two reasons we choose to use the pure water ice thermal conductivity and heat capacity: we take $k_s = 2.3 \text{ W m}^{-1} \text{ K}^{-1}$ (for water ice at 273 K, c.f. Hobbs, 1975) and $c_p = 2 \times 10^3 \text{ J kg}^{-1} \text{ K}^{-1}$ (Hobbs, 1975). The assumption of having the same solid material inside and outside the reservoir was also a necessary assumption in order to solve the Stefan problem with thermal transfer outside the reservoir. However, the trends of the results are not expected to be significantly different if one takes into account the salts in the ice crust. S_c can be written as a function of n_c and R , the reservoir radius:

$$S_c = R \left(1 - (1 - n_c)^{1/3} \right) \quad (18)$$

2.3. Cryomagma eruption

2.3.1. Fracture propagation to the surface

For an overpressure ΔP_c , the tensile stress applied on the reservoir wall is high enough to initiate a fracture (McLeod and Tait, 1999). Nevertheless, the fracture propagation needs to overcome the difficulty due to the negative buoyancy of the liquid with respect to the surrounding ice. Although the denser fluid is driven upward by the reservoir overpressure (Fagents, 2003), the cryomagma buoyancy tends to transport it downward. In our case the former effect is dominant. Indeed, with $\Delta\rho$ the density difference between the cryomagma and the surrounding ices (never exceeding 100 kg m^{-3} in our case), and with $g \simeq 1.315 \text{ m s}^{-2}$, for an overpressure ΔP_c in the reservoir of order of 10 MPa (that is the typical overpressure value obtained for $H = 10 \text{ km}$), the ratio between the buoyancy and pressure force is of order of 0.1. Fracture propagation is then driven by the excess pressure-dominated flow (Rubin, 1995).

Fracture propagation is also limited by the host medium resistance: the crack-tip stress intensity factor K_t must exceed the ice fracture toughness K_c for the fracture to propagate (Lister and Kerr, 1991; Rubin, 1993). If $K_t \gg K_c$, the fracture propagation velocity can theoretically reach 40% of the speed of sound in the ice, but in reality it is limited by the velocity of the fluid in the fracture (Lister and Kerr, 1991). If

the overpressure ΔP is uniform in the fracture, which is valid because the isostatic pressure is two orders of magnitude lower than the overpressure in the reservoir, the crack-tip stress intensity factor is given by (Lister and Kerr, 1991):

$$K_t = \Delta P \sqrt{H} \quad (19)$$

which gives $K_t \simeq 31 \text{ MPa m}^{1/2}$ for $\Delta P = 1 \text{ MPa}$ and a fracture length $H = 1 \text{ km}$ and $K_t \simeq 316 \text{ MPa m}^{1/2}$ for $\Delta P = 10 \text{ MPa}$ and a fracture length $H = 10 \text{ km}$, which are the ranges of depth and pressure used in this study. On the other hand, the ice fracture toughness K_c measured by Litwin et al. (2012) lies in the range $0.05 < K_c < 0.2 \text{ MPa m}^{1/2}$.

Here $K_t \gg K_c$, so fracture propagation would occur at very high velocity, but is actually limited by the slower flow velocity of cryomagma into the fracture and cannot exceed it (Lister and Kerr, 1991). We show in section 3.2 that the cryomagma travels at velocities of a few to tens of meters per second, which although slower, still allows a very quick fracture propagation. As a comparison, Traversa et al. (2010) showed that terrestrial vertical basaltic dikes propagated at velocities of order of 1 m s^{-1} during the Piton de la Fournaise eruption in 2003. As the fracture propagation velocity depends on the fluid velocity and host medium fracture toughness K_c (Lister and Kerr, 1991; Rubin, 1993), higher velocities are expected for water cryomagmas than for basalt. Thanks to the high flow velocity within the fracture, it is likely that fluid will be delivered to the surface before it freezes (Craft et al., 2016; Quick and Marsh, 2016).

Once a fracture is created, the pressure necessary to maintain it open writes (Sigurdsson et al., 1999):

$$P_{open} = \frac{E}{2(1-\nu^2)} \frac{b}{a} \quad (20)$$

where ν is the Poisson's number, E is the Young's modulus, and a and b are the major and minor semi-axis of the dike. For $a = 100 \text{ m}$ and $b = 1 \text{ m}$ (the typical values used in this study), $E \leq 10^9 \text{ Pa}$ and $\nu \simeq 0.325$, we obtain $P_{open} \lesssim 5 \times 10^7 \text{ Pa}$, which is well under the critical pressure inside the reservoir (see section 3.2).

Another mechanism that could play a role in the opening or closing of fractures in the ice is the diurnal stress generated on the ice crust by the tides. It has been proposed that tidal activity on Europa could be linked with the orientation of linear features observed at the surface (Greenberg and Geissler, 2002). Wahr et al. (2009) showed that tidal activity can generate stresses up to 90 kPa at some points of the surface, which is one order of magnitude lower than σ_c (Litwin et al., 2012). As the period of the tides on Europa is 3.55 days, this might affect the fracture opening or closing. Nevertheless, our results show that eruption duration

should not exceed 20 hours (see Sec. 3.2), so eruption of a cryomagma reservoir seems possible during a tidal cycle and especially when tidal stress contributes to the opening. Also, ice fracturing could be facilitated by the extensional constraints predicted in Europa’s ice shell by Nimmo (2004a) due to the global cooling of the moon, and that should generate stresses around few to 20 MPa. This tangential stress is expected to be maximum around 2 km deep for a 30 km thick ice shell (Nimmo, 2004a).

2.3.2. Cryomagma flow

The nature of the liquid flow in the open fracture is given by the Reynolds number Re :

$$Re = \frac{\rho_l U b}{\mu} \quad (21)$$

where U is the mean velocity of the flow in the fracture, b is the fracture width, ρ_l is the liquid density and μ is the pure or briny liquid water dynamic viscosity. The transition between laminar and turbulent flow occurs when $Re \simeq 10^3$ (Bejan, 1993; Bird et al., 1960 (First Edition), i.e. the flow is in turbulent regime for velocities greater than approximately 10^{-4} to 10^{-3} m s^{-1} as a function of the conduit geometry. Moreover, Quick and Marsh (2016) recently studied the heat transfer from liquid water cryomagma rising through the uppermost 10 km of Europa’s ice shell. They showed that the minimum fluid velocity required to reach the surface before freezing is around $2.5 \times 10^{-2} \text{ m s}^{-1}$ for a 4 m wide and 10 km long tabular fracture, and of order of $8 \times 10^{-4} \text{ m s}^{-1}$ for a 12 m radius and 10 km long cylindrical conduit. For this reason, we make the hypothesis that the ascending flow is turbulent, and this hypothesis will be verified afterward (see section 3.2). This assumption is also in agreement with the results from Craft et al. (2016) where they find the flow would be turbulent for pure water rising up a 10 to 100 m wide tabular fracture.

When a cryomagnetic reservoir fails, the fracture created has a tabular shape (McLeod and Tait, 1999). However, an elongated, planar fracture might evolve to become a pipe-like conduit, as observed on Earth (Quick and Marsh, 2016). In the case of Europa, we have no information about the conduit geometry, so we consider two different geometries: a fracture with an elongated rectangular cross-section or a pipe-like conduit with a circular cross-section. In the following, we consider the more general hydraulic diameter D_h , that is defined by Bejan (1993) as a length scale that can replace the diameter in the flow velocity calculations in order to make them applicable to all fracture or conduit geometries:

$$D_h = \frac{4A}{p} \quad (22)$$

where A is the cross-sectional area of the fracture or conduit and p its perimeter.

At Europa's surface, the pressure is nearly zero Pascal (Hall et al., 1995), and the pressure in the reservoir is $P_{tot} = P_0 + \Delta P$ where $P_0 = \rho_s g H$. Upward flow is maintained by the pressure difference between the two ends of the conduit. The mean flow velocity results from a force balance in the fracture (Bejan, 1993; Bird et al., 1960 (First Edition)). The total friction applied on the fracture walls is $\tau_w p H$ where τ_w is the shearing stress on the walls and p and H are respectively the fracture perimeter and length. The vertical momentum balance for a fully developed and incompressible flow gives:

$$A(P_{tot} - \rho_l g H) = \tau_w p H \quad (23)$$

The shearing stress τ_w is classically expressed as a function of the Fanning friction factor f in turbulent flow (Bird et al., 1960 (First Edition)):

$$\tau_w = \frac{1}{2} f \rho_l U^2 \quad (24)$$

The Fanning factor f depends on the geometry and roughness of the conduit. Since we have no information on the fracture roughness, we take a mean value of $f = 0.01$ (Bejan, 1993; Bird et al., 1960 (First Edition)) which is an acceptable approximation because the order of magnitude of this factor should not vary for the Reynolds numbers relevant here. Combining Eq. (22), (23) and (24), we obtain the expression for the mean ascent velocity:

$$U = \sqrt{\frac{D_h (P_{tot} - \rho_l g H)}{2 f H \rho_l}} \quad (25)$$

Knowing the velocity of the flow and the fracture/conduit cross section, we can deduce the cryomagma effusion rate at the surface. By integrating the effusion rate, we can also determine the total erupted volume during a cryovolcanic event.

The method used is summarized in the flowchart of Fig. 4. Starting from the initial overpressure in the reservoir ΔP_e (Eq. (12)), n_e is derived from Eq. (13) and the remaining liquid volume in the reservoir after freezing V_f derived from Eq. (4). These initial conditions allow us to calculate the flow velocity at the beginning of the eruption from Eq. (25) and the volume of cryomagma erupted at the surface during a time step dt . At each time step, the effusion of cryomagma modifies the liquid density in the reservoir because P_{tot}

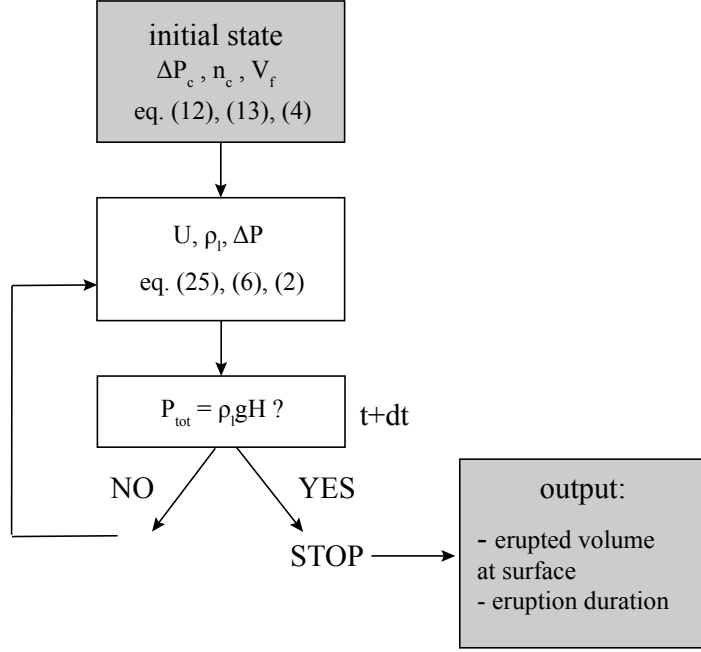


Figure 4: Numerical process used to solve the time dependence of our model.

is decreasing. The density of the liquid at time $t + dt$ and the pressure in the reservoir after decompression are given respectively by Eq. (6), and Eq. (2). The velocity U is then modified accordingly. To solve this time dependent problem we use a Runge-Kutta method. The eruption stops when the pressure in the reservoir equals the hydrostatic pressure due to weight of the water column in the fracture ($P_{tot} = \rho_l g H$) and U decreases to zero velocity.

3. Results

3.1. Pre-eruptive freezing and triggering of an eruption

The critical fraction of freezing cryomagma n_c necessary to trigger an eruption depends on the density contrast between the liquid in the reservoir and the surrounding ice ρ_w/ρ_i (Eq. (13)), but also on the reservoir depth. Fig. 5(a) shows n_c as a function of reservoir depth and cryomagma composition. As previously stated, for the briny cryomagma, we used $\rho_l = 1180 \text{ kg m}^{-3}$ and $\rho_s = 1130 \text{ kg m}^{-3}$ (see Table 1 and Kargel 1991). Fig. 5(b) shows the value of the critical overpressure ΔP_c generated by the freezing of a fraction n_c of the reservoir as a function of the depth of the reservoir.

A good estimate of the relative volume change of a spherical reservoir surrounded by an elastic medium under overpressure ΔP_c is given by $\frac{\Delta V}{V} = \frac{1}{K} \Delta P$ where $K = \frac{1}{3} \frac{E}{(1-2\nu)}$ is the ice bulk modulus. With $E \simeq 9$ GPa at -5°C (Hobbs, 1975) and $\nu \simeq 0,35$ at -5°C (Hobbs, 1975), thus $K = 10$ GPa. We calculate the relative volume variation for different reservoir depths and critical overpressures and we find at most 0.005 (for a maximum $\Delta P_c = 30$ MPa, see Fig. 5(b)), compared to the relative ice to reservoir volume of order of 0.3. We hence neglect the elastic deformation of the reservoir wall in the following.

For the briny cryomagma, a larger fraction of liquid is required to freeze in order to reach the critical pressure in the reservoir than for pure water. Figure 5(a) shows that the critical fraction of briny cryomagma n_c is more than twice that of pure water. In fact, n_c depends on the density contrast between the liquid in the reservoir and the surrounding ice ρ_w/ρ_i (Eq. (13)), which is higher for pure liquid water and ice. This means that briny mixtures are less efficient than pure liquid water in generating an overpressure in the reservoir. In any case, the maximum fraction n_c reaches 25% of the reservoir volume for the deepest possible reservoirs compatible with our starting hypothesis that the volume ranges from 10^6 to 10^{10} m³.

In order to estimate, to first order, the size and depth of the reservoir that may produce observable flow features at Europa surface, we conducted a parametric study varying the reservoir depth, H , and the total reservoir volume, V . We vary the reservoir radius from 50 m to 1300 m, which corresponds to volumes ranging from 10^6 to 10^{10} m³. These volumes cover a large range because of the lack of information on putative reservoir geometry. The smaller reservoirs ($R = 50$ m) might be consistent with small features at Europa's surface, and the larger reservoirs ($R = 1300$ m) correspond to typical terrestrial magma reservoirs, which commonly range from 1 to 9 km (Sigurdsson et al., 1999). We do not rule out the possible existence of larger reservoirs, especially in the case of sheet-like reservoirs as it is observed on Earth (Sigurdsson et al., 1999).

Knowing the frozen fraction n_c , we can deduce the thickness S_c of cryomagma necessary to freeze in order to trigger an eruption using Eq. (18). Fig. 6 shows S_c for the pure and briny cryomagmas (respectively Fig. 6(a) and 6(b)) as a function of the reservoir depth and volume. The solidification of a layer of thickness S_c takes a time τ_c (see Fig. 7).

In agreement with the results in Fig. 6, the freezing time-scale also increases for briny cryomagmas. S_c increases with the addition of salts by a factor ~ 2 , and τ_c increases by a factor of ~ 10 for the largest and deepest reservoirs. Also note that S_c and τ_c vary as a function of the temperature difference between the reservoir interior and the surrounding ice (respectively T_m and T_{cold}). The difference $T_m - T_{cold}$ is greater

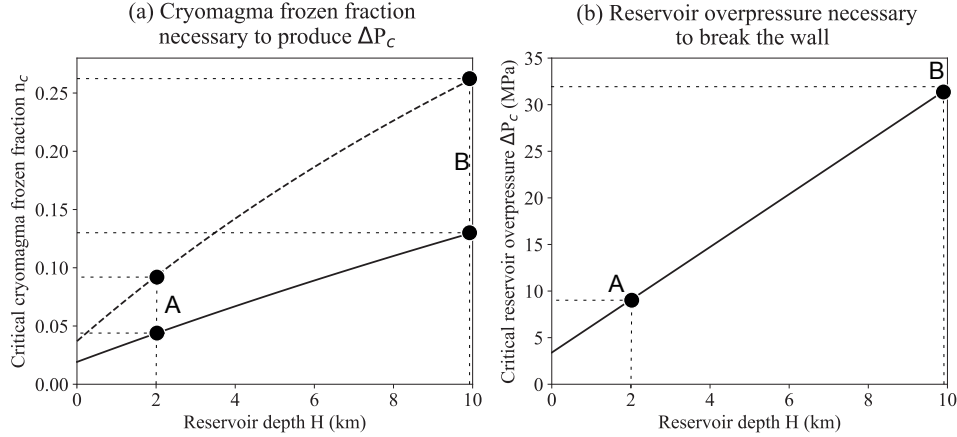


Figure 5: Criteria needed to fracture the reservoir wall: (a) the frozen fraction n_c and (b) the overpressure ΔP_c for pure water (solid line) and briny cryomagma (dashed line). We take two examples of reservoirs, named A and B (see text for details). Reservoir A has a medium size ($R = 600$ m, $V = 10^9$ m³) and is located 2 km below the surface and reservoir B is the largest reservoir explored in this study ($R = 1.3$ km, $V = 10^{10}$ m³) located 10 km below the surface.

for near-surface reservoirs, where the ice temperature decreases toward a value of order of 100 K.

We take two examples of reservoirs, named hereafter reservoirs A and B. Reservoir A has a medium size ($R = 600$ m, $V = 10^9$ m³) and is located 2 km below the surface, a depth at which Nimmo (2004a) predicted an enhanced tensile state of stress in a cooling and thickening ice shell, from the thermal contraction of the ice shell and its expansion due to the ice—water volume change. This peak extensional stress could help to open a reservoir located around 2 km beneath the surface in a 30 km thick ice shell, even though this effect is not taken into account in this study. Reservoir B is the largest and deepest reservoir explored in this study ($R = 1.3$ km, $V = 10^{10}$ m³), located at 10 km depth where melting could occur due to tidally heated warm ice plumes (Tobie et al., 2003). For a plausible briny cryomagma, reservoir A needs to freeze 8% of its volume (see Fig. 5(a)), which corresponds to a ~ 20 m thick layer (see Fig. 6(b)) to trigger an eruption. This process takes ~ 20 years (see Fig. 7(b)). In the case of reservoir B, a larger volume fraction of briny cryomagma is necessary to freeze because of the greater reservoir depth ($\sim 26\%$, see Fig. 5(a)), corresponding to a layer thicker than 100 m (see Fig. 6(b)) that takes more than 1000 years to freeze (see Fig. 7(b)).

3.2. The eruption of cryomagma

We first look at the time evolution of the reservoir pressure and flow velocity for reservoir A (volume $V = 1$ km³, depth $H = 2$ km, filled with briny cryomagma) connected to the surface by a fracture of rectangular cross-section with area $A = 100$ m² and perimeter $p = 200$ m, arbitrarily chosen because we have

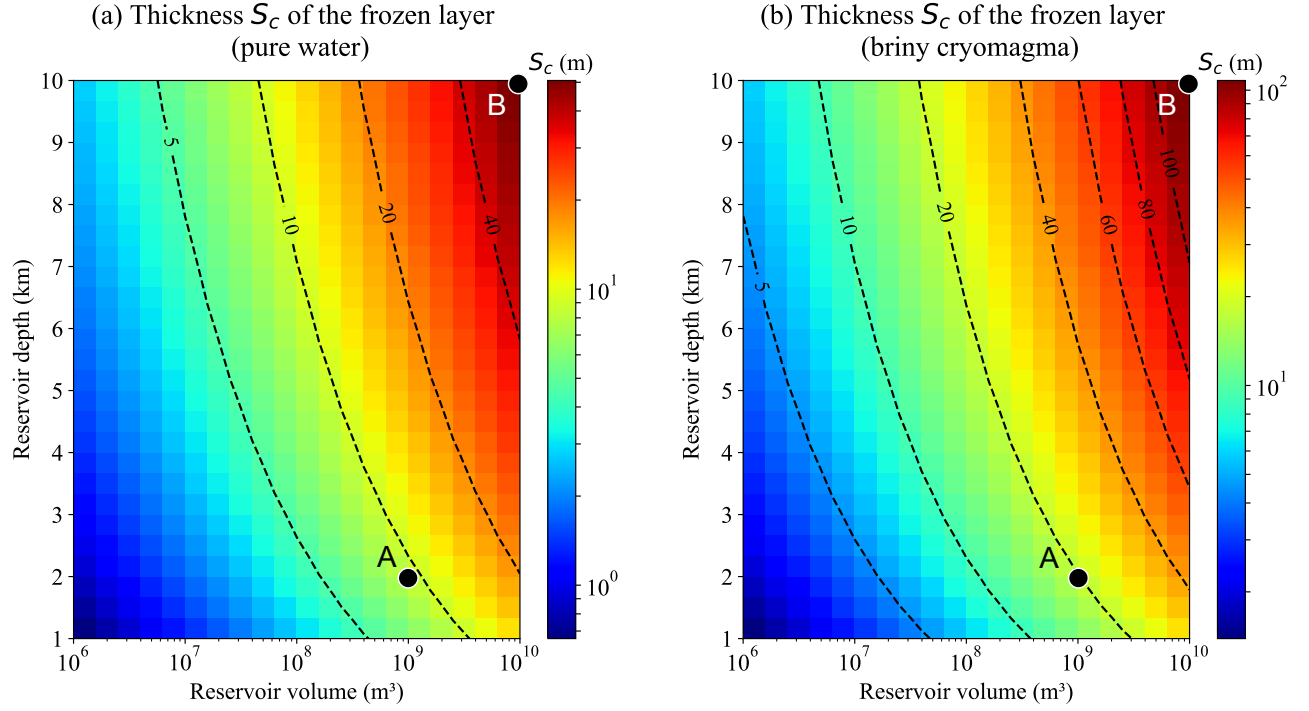


Figure 6: Thickness S_c of the frozen cryomagma as a function of reservoir depth and volume for (a) pure water and (b) briny cryomagma. Each color square represents an output from one model run. Reservoir A has a medium size ($R = 600 \text{ m}$, $V = 10^9 \text{ m}^3$) and is located 2 km below the surface and reservoir B is the largest reservoir explored in this study ($R = 1.3 \text{ km}$, $V = 10^{10} \text{ m}^3$) located 10 km below the surface.

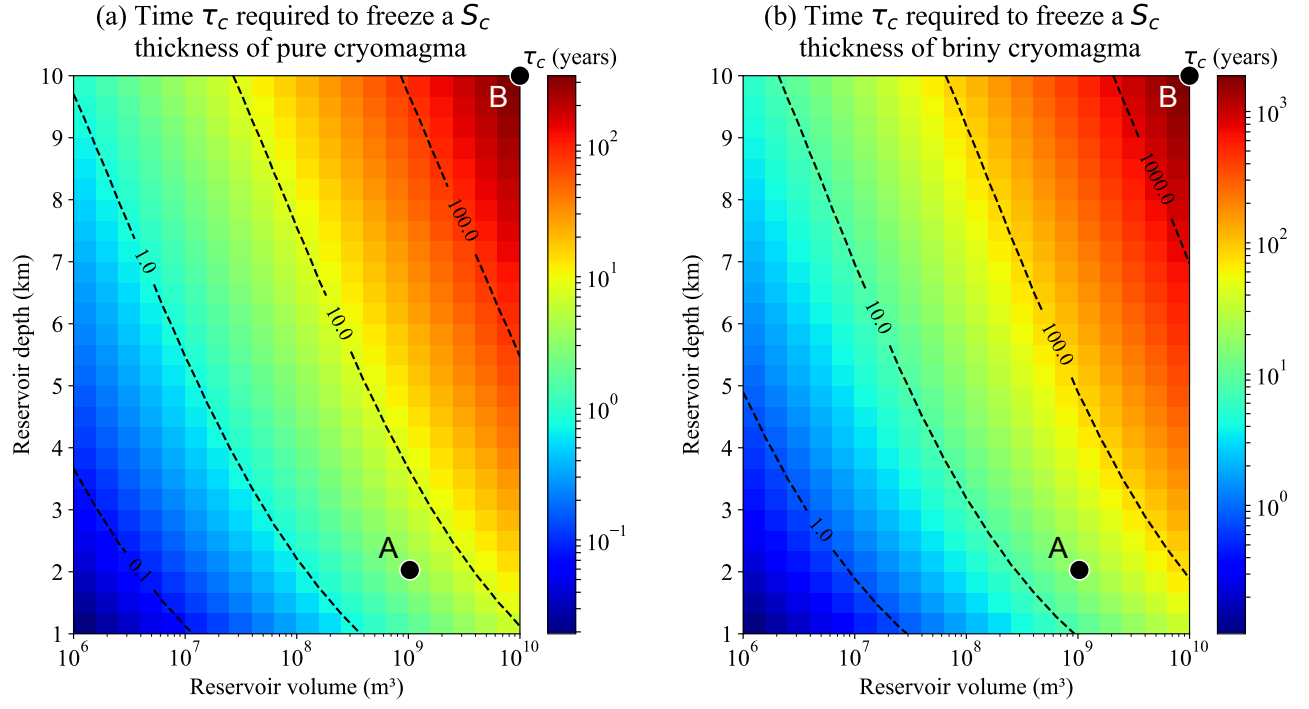


Figure 7: Time τ_c required to freeze (a) a pure and (b) a briny cryomagma layer of thickness S_c as a function of reservoir depth and volume. Each color square represents an output from one model run. Reservoir A has a medium size ($R = 600 \text{ m}$, $V = 10^9 \text{ m}^3$) and is located 2 km below the surface and reservoir B is the largest reservoir explored in this study ($R = 1.3 \text{ km}$, $V = 10^{10} \text{ m}^3$) located 10 km below the surface.

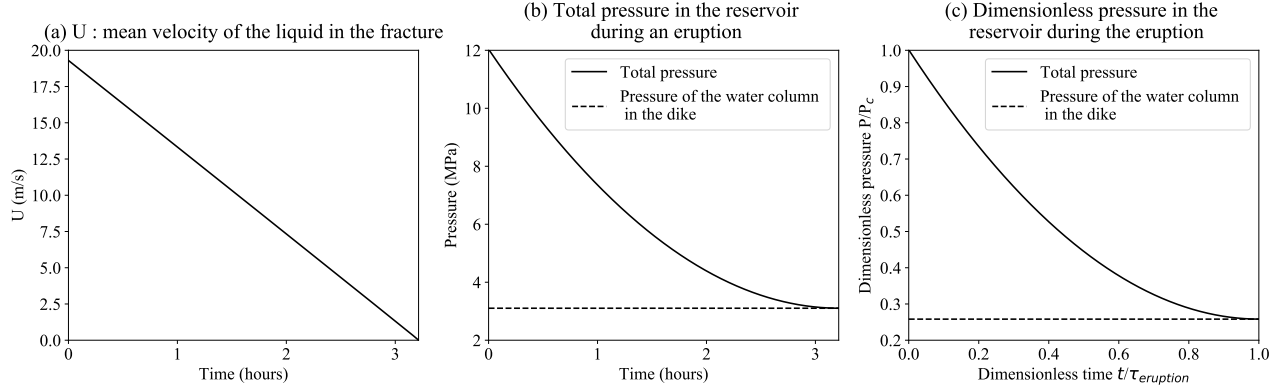


Figure 8: Evolution of (a) the mean flow velocity, (b) the pressure in the reservoir during an eruption which begins when the reservoir opens and ends when the reservoir is back at hydrostatic pressure and (c) the dimensionless pressure. These results are obtained for the reservoir A (volume $V = 1 \text{ km}^3$, depth $H = 2 \text{ km}$) filled with briny cryomagma and connected to the surface by a fracture of rectangular cross-section with area $A = 100 \text{ m}^2$ and perimeter $p = 200 \text{ m}$.

no constraints on European fracture widths when they are held open. The influence of the cross-sectional area and geometry is discussed below.

Fig. 8(a) shows that the average briny or pure cryomagma velocity is a maximum ($\simeq 20 \text{ m.s}^{-1}$, corresponding to a Reynolds number $Re \simeq 10^8$) when the reservoir opens, at the beginning of the eruption, in accordance with the greatest ΔP value acting at that time. Only at the very end of the eruption is the flow in the laminar regime, with velocity less than 10^{-3} m s^{-1} . The assumption of turbulent flow is thus validated.

Fig. 8(b) shows the pressure evolution during the course of the eruption, when cryolava is erupted at the surface. The eruption ends when the pressure inside the reservoir equals the hydrostatic pressure due to the weight of the fluid column in the conduit. In the particular case of reservoir A in Fig. 8, the eruption lasts only one hour. This general trend is common to all cases modeled here ($\tau_{eruption}$ varying between 3 min and 20 h and P_c varying between 5.6 and 59 MPa). Fig. 8(c) shows the dimensionless pressure evolution and time obtained with these ranges of parameters.

We now examine the influence of conduit geometry, reservoir depth and volume on eruption duration and erupted volumes. We conducted calculations for cylindrical conduits as investigated by Quick and Marsh (2016). The cross-sectional geometry of the elongated fracture or pipe-like conduit has an influence on the cryomagma flow: flow velocity increases with A/p where A is the cross-sectional area and p is the perimeter. In our study, we consider that the fracture or conduit has a constant A/p ratio with height above the reservoir. The fracture geometry is a parameter fixed in our model and does not vary with the chamber volume or depth. Fig. 9 (a) shows the flow velocity at the beginning of the eruption as a function of A/p for the parameters

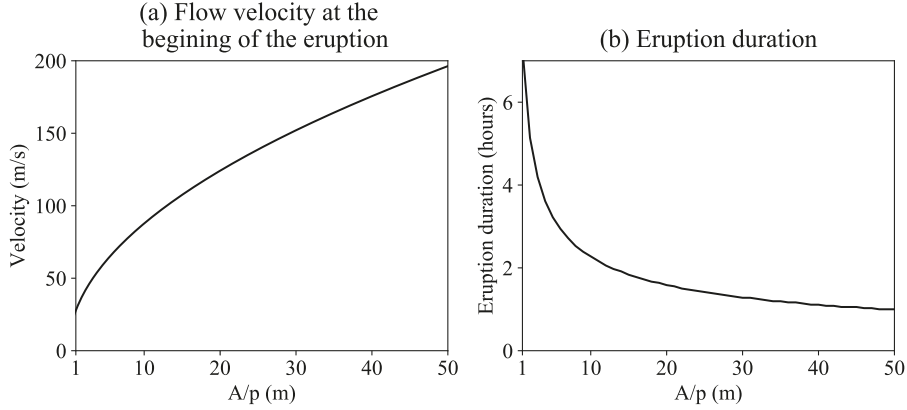


Figure 9: (a) Flow velocity at the beginning of an eruption and (b) eruption duration as a function of A/p (where A is the cross-sectional area and p is the perimeter of the conduit) for pure liquid water, $V = 10 \text{ km}^3$ and $H = 2 \text{ km}$.

$V = 10 \text{ km}^3$ and $H = 2 \text{ km}$. The maximum value explored here $A/p = 50 \text{ m}$ corresponds to a 100 m radius cylindrical conduit. Fig. 9 (b) shows how the eruption duration varies with A/p for fixed reservoir volume and depth. Moreover, for a fixed A/p ratio, the cryomagma volumetric flow rate in the fracture is proportional to the cross-sectional area of the conduit. This effect is of lesser importance and not explored further.

As described in section 2.3.2, our model allows us to obtain the eruption duration τ_{eruption} and the total erupted volume V_e as a function of H and V . For the simulations given in Fig. 10, we assume that the cryomagma rises through a tabular fracture with a 100 m^2 cross sectional area. These results are obtained for pure water and briny cryomagma and ice. The eruption duration and erupted volume obtained for the briny solution are slightly greater than those obtained for pure water, but the difference never exceeds a few percent (see Fig. 10). This effect is independent of the reservoir volume but increases with the reservoir depth.

As we can see in Fig. 10(a) and (c), reservoir A ($R = 600 \text{ m}$, $V_e = 10^9 \text{ m}^3$) erupts in ~ 1 hour, but a very small cryomagma volume of $3 \times 10^6 \text{ m}^3$ is erupted (see Fig. 10(b) and (d)). In the case of reservoir B ($R = 1.3 \text{ km}$, $V_e = 10^{10} \text{ m}^3$), the eruption lasts ~ 20 hours (see Fig. 10(a) and (c)) and $\sim 10^8 \text{ m}^3$ of cryomagma is erupted (see Fig. 10(b) and (d)). More generally, for the range of reservoir and cryomagma parameters investigated here, the total volume emitted at the surface ranges from 10^3 to 10^8 m^3 , which represents 0.1 to 1% of the reservoir. These volumes would create relatively small features at the surface, but we do not rule out the possible existence of larger reservoirs. The results also show that the eruption duration varies from

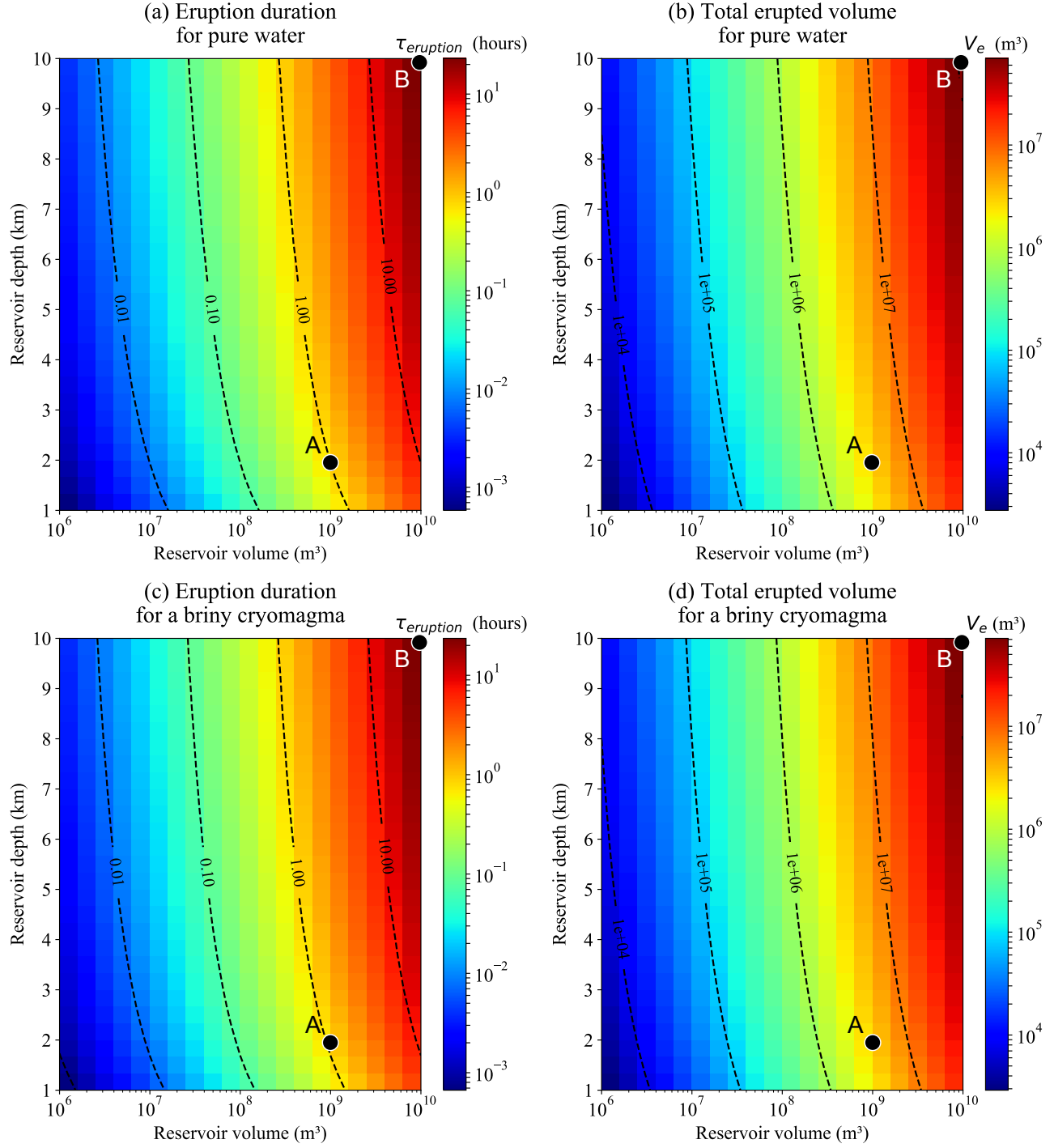


Figure 10: (a) Eruption time-scale and (b) total erupted volume at the surface during an eruption as a function of reservoir depth H and volume V for pure liquid water, and the same results in (c) and (d) for a briny cryomagma. These results are obtained for liquid ascending through a tabular fracture with a 100 m \times 1 m cross section. Each color square represents an output from one model run. Reservoir A has a medium size ($R = 600$ m, $V = 10^9$ m³) and is located 2 km below the surface and reservoir B is the largest reservoir explored in this study ($R = 1.3$ km, $V = 10^{10}$ m³) located 10 km below the surface.

a few minutes to a few tens of hours for the largest reservoirs. These short time-scales are in agreement with the hypothesis we made previously that the cryomagma rises isothermally through the fracture or pipe-like conduit. In fact, Quick and Marsh (2016) predicted that cryomagma ascent would be isothermal if it travels faster than 10^{-2} m s^{-1} , which is indeed true for the cases we investigate here.

3.3. *Effect of the temperature gradient in the ice crust*

In this study, we consider an ice shell with an outer 10 km conductive layer. The temperature at Europa's surface varies during the day between 80 to 130K (Spencer, 1999) so we take a mean value around 100 K. However, the temperature profile deeper in the ice shell is less well known and may depend on several factors. First of all, the conductive ice layer might be thicker or thinner than the 10 km thickness considered here depending on the heat flux coming from Europa's interior (Tobie et al., 2003; Quick and Marsh, 2015), and the temperature at the base of the conductive layer might be higher, around 250 K after Tobie et al. (2003). Finally, the presence of warm ice plumes could modify locally the temperature around the reservoir, especially if the warm plume is at the origin of the melting of the reservoir (Sotin et al., 2002; Mitri and Showman, 2008; Schmidt et al., 2011). Hence, it could be relevant to consider a second temperature gradient in the conductive lid, varying between 100 to 250 K.

We therefore consider the case of a temperature gradient varying from 100 K at the surface to 250 K at the bottom of the conductive ice layer following Tobie et al. (2003) (at 10 km depth here): $T(H) = 100 + \frac{150}{10^4} H$, and we modify all dependent parameters accordingly. Fig. 11 shows the time required to freeze the fraction n_c of the reservoir for a temperature gradient varying from 100 K to 250 K. The freezing time-scale is slightly increased compared with the colder temperature gradient, especially for the deepest chambers, but the order of magnitude of the freezing time is similar than when considering lower temperature gradient in the framework of our model (see Fig. 7).

4. Discussion

4.1. *Reservoir freezing and life times*

The necessary time to fracture the reservoir has been calculated with the approximation of a purely elastic surrounding ice. Nevertheless, as the chamber freezes, heat exchange with the surrounding of the reservoir might affect the rigidity of the walls. Fig. 12 shows the temperature around the reservoir after a time τ_c as a function of the reservoir depth (for a 100 K - 200 K temperature gradient). The temperature around

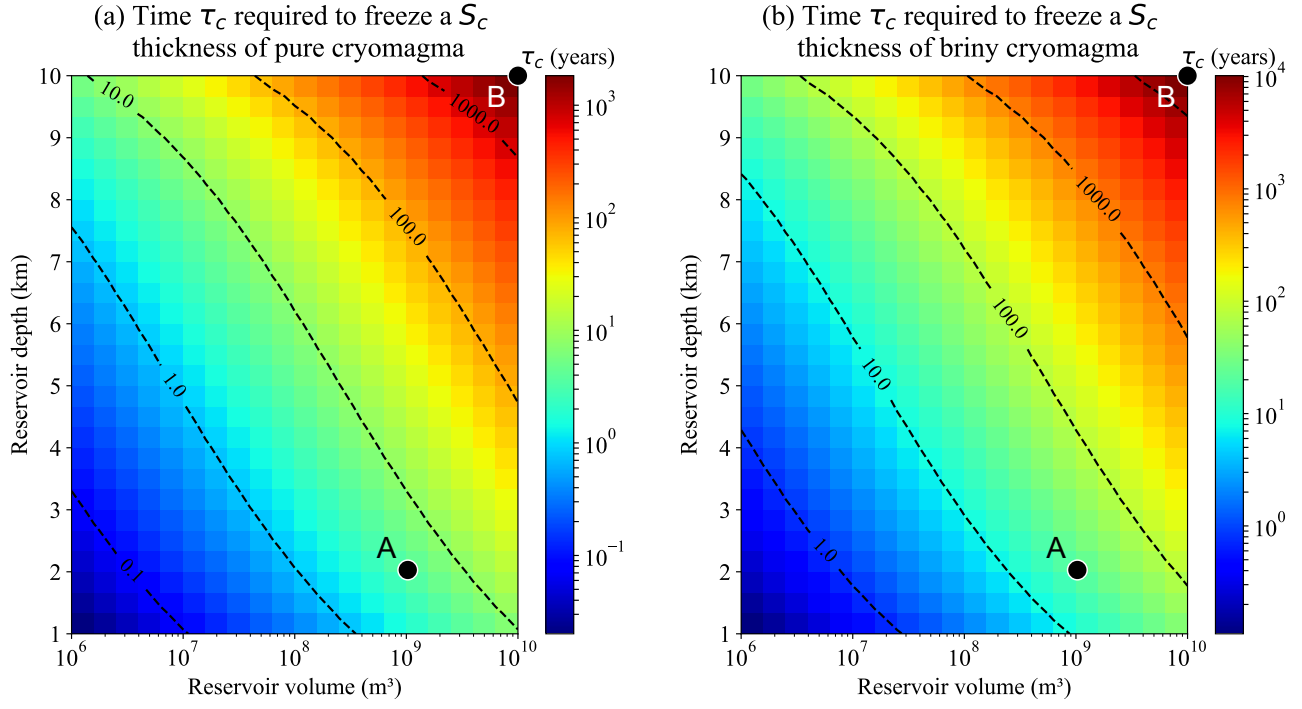


Figure 11: Time τ_c required to freeze (a) a pure and (b) a briny cryomagma layer of thickness S_c as a function of reservoir depth and volume for a temperature gradient of 100 to 250 K. Each color square represents an output from one model run. Reservoir A has a medium size ($R = 600$ m, $V = 10^9$ m^3) and is located 2 km below the surface and reservoir B is the largest reservoir explored in this study ($R = 1.3$ km, $V = 10^{10}$ m^3) located 10 km below the surface.

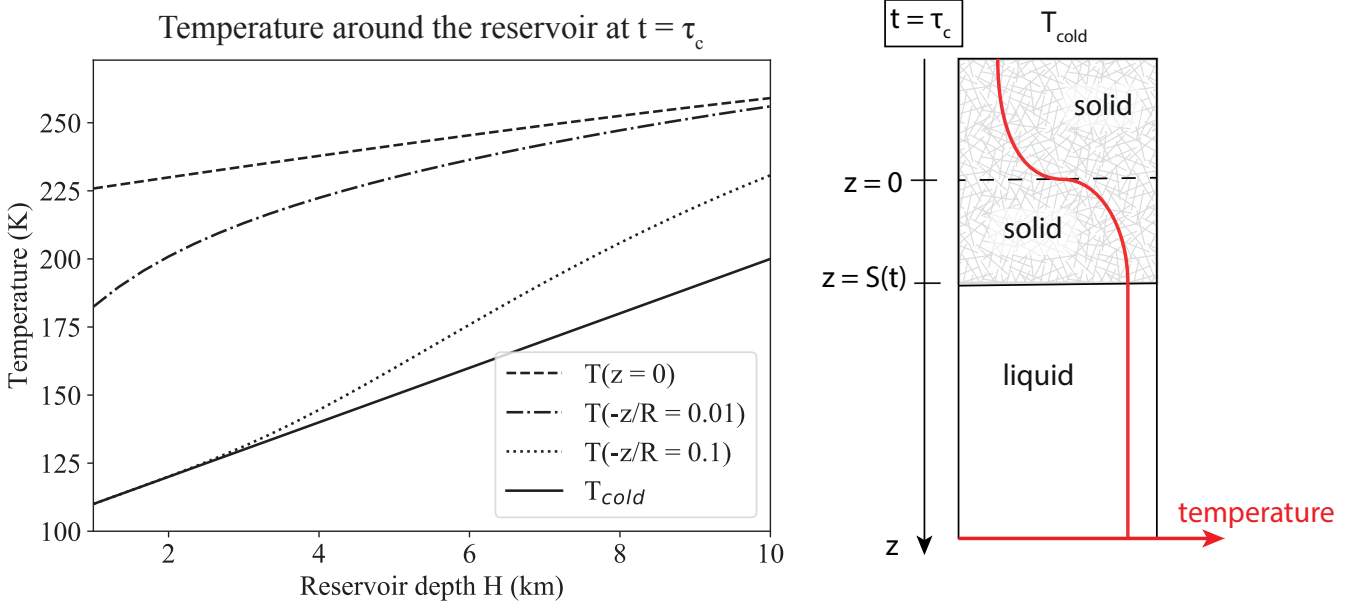


Figure 12: Temperature around the reservoir at time τ_c at four different locations: $z = 0$ (reservoir wall), $-z/R = 0.01$, $-z/R = 0.1$, and $z \rightarrow -\infty$ (T_{cold} , plain line).

the chamber is calculated at the reservoir wall where $z = 0$, far from the reservoir where $z \rightarrow -\infty$ and the temperature is constant at $T = T_{cold}$, and at two dimensionless locations such as $-z/R = 0.01$ and 0.1 . From Fig. 12, we can see that the temperature quickly decreases moving away from the reservoir (decreasing z), such that the surrounding ice should remain sufficiently cold to behave elastically.

The most important parameter to describe the ice behavior around the reservoir is the Maxwell relaxation time of the ice τ_M . If a stress is applied to the ice on a time-scale shorter than τ_M , the material behaves in an elastic manner, and at times longer than τ_M , it behaves as a viscous material. The Maxwell relaxation time is expressed as $\tau_M = \mu_{ice}/E$ where μ_{ice} is the ice viscosity and E the Young's modulus. We know from Gammon et al. (1983) and Petrenko and Whitworth (2002) that $E \simeq 9$ GPa, and μ_{ice} is temperature dependent (Hillier and Squyres, 1991):

$$\mu_{ice} = 10^{14} \exp \{25.2 (273/T(K) - 1)\} \text{ Pa s} \quad (26)$$

Fig. 13 shows the Maxwell time of pure water ice as a function of the temperature, using Eq. (26). The Maxwell relaxation time-scale might be compared to the freezing time of the reservoir. Rapid freezing does

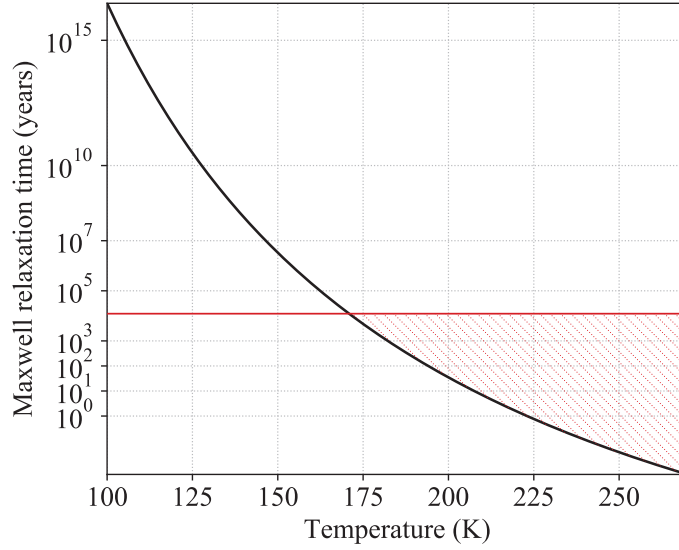


Figure 13: Maxwell relaxation time $\tau_M = \mu_{ice}/E$ of pure water ice as a function of the temperature. The red line represents the maximum freezing times obtained for the range of chamber volumes and depths considered in this study. The region hatched in red shows the temperatures for which a reservoir is expected to behave in a viscous manner, which is not modeled in the present study.

not allow the reservoir wall to accommodate the pressure by viscous relaxation and thus the wall fractures in an elastic manner. Our results indicate that a reservoir takes a few hundred to 10^4 years to freeze before triggering the eruption, so it is expected that the warmest and largest reservoir could have a freezing time-scale exceeding the Maxwell time of the ice (i.e. $\tau_c > \tau_M$, see the region hatched in red in Fig. 13). Using the results obtained in section 3, we show in Fig. 14 the freezing time-scale τ_c normalized with the Maxwell time of the ice surrounding the reservoir. Reservoirs for which $\tau_c/\tau_M < 1$ are expected to react elastically to the stress generated by the cryomagma freezing, and so our assumption of elastic material is valid in this case. For the reservoirs in the $\tau_c/\tau_M > 1$ region, the viscous response of the ice should be taken into account to obtain a more realistic pre-eruption model. This is not investigated here because it would require further modeling, but this effect will extend the time required to fracture the reservoir and propagate a crack, or maybe prevent the eruption for some extreme cases.

In a previous work, Kalousová et al. (2014) showed that a lens containing a fraction of pure liquid water within Europa's shell should be efficiently transported downward due to propagation of porosity waves through the ice. Their results are obtained for ice permeability ranging from 10^{-10} to 10^{-8} m², and they showed that pure liquid water can be transported to the internal ocean in 10^3 to 10^5 years. As discussed in their study and predicted by Schmidt et al. (2011), the liquid water might also be stored at some depth if

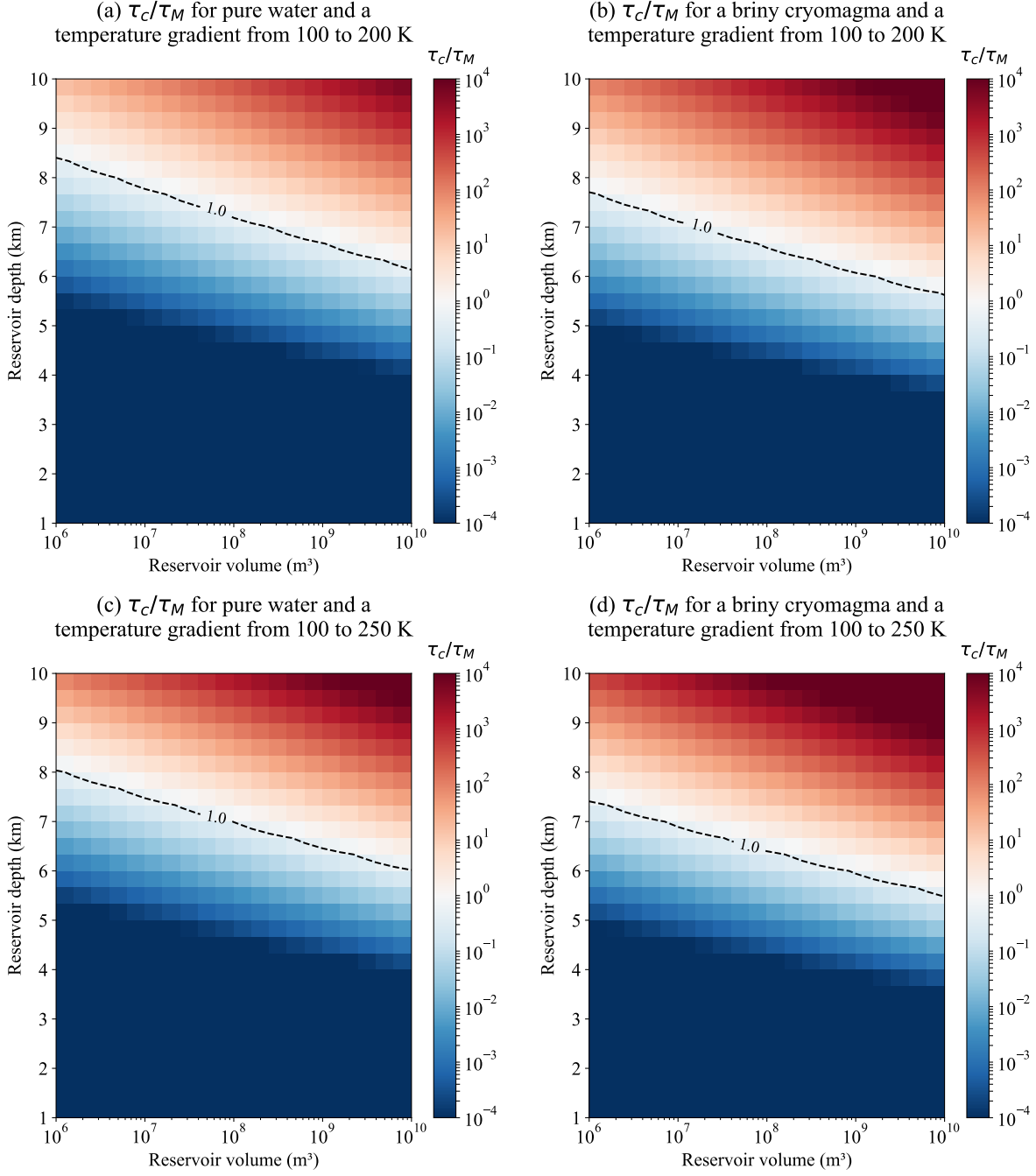


Figure 14: τ_c/τ_M dimensionless time, where τ_c is the reservoir freezing time-scale and τ_M is the Maxwell time of the surrounding ice, as a function of the reservoir volume V and depth H . The temperature gradient in the ice is assumed linear, with temperature rising from a minimum at the surface to a maximum 10 km deep. The reservoir will behave elastically when $\tau_c/\tau_M < 1$ (in blue).

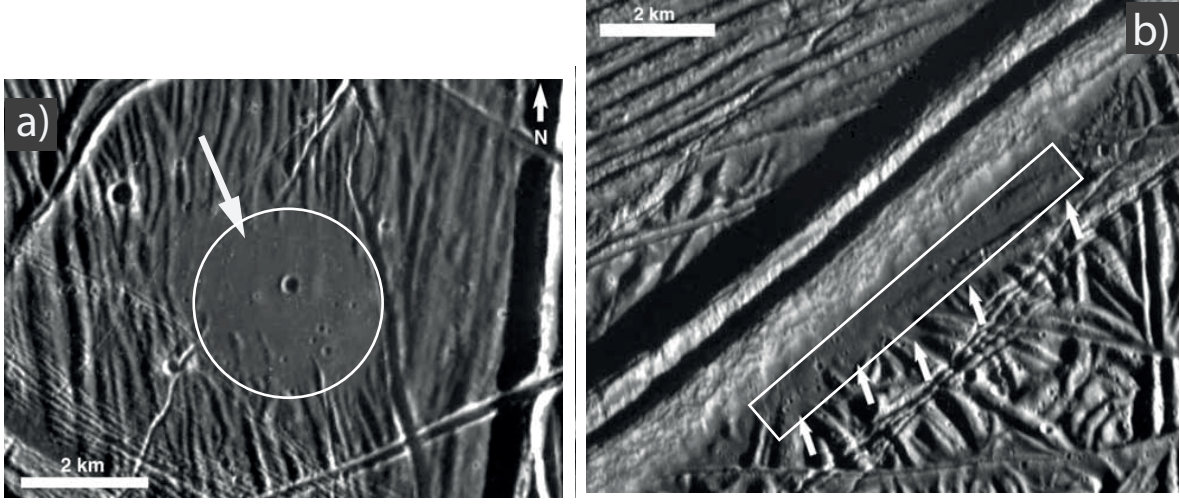


Figure 15: Circle and rectangle delineate the approximate surface areas of possible fluid effusions located in (a) 6°N, 327°W (Galileo image from orbit E4) and (b) 15°N, 273°W (Galileo image from orbit E6).

it encounters a salt rich ice layer. Our results show that the freezing of the reservoir should take less than 10^3 years for pure liquid water and 10^4 years for a briny mixture, and therefore the eruption should not be prevented by the reservoir percolation to the ocean.

4.2. Observational constraints

It is beyond the scope of the present paper to conduct precise topographic reconstruction or detailed geomorphologic interpretations, but we nevertheless use the output of our model to interpret to first order the origin of two smooth deposits on Europa. We measured the approximate area of the smooth deposits shown in Fig. 15 and obtained an area of approximately $7 \times 10^6 \text{ m}^2$ for each of these two features. Various studies have estimated double ridge heights from around 100 to 300 m (Greeley et al., 1998; Head et al., 1999; Dameron and Burr, 2018). If we consider that the double ridge of Fig. 15(b) is 100 to 300 m high, it seems plausible that the smooth deposit flanking the ridge is a few meters thick. Moreover, a thickness less than 1 meter would be hard to detect at 30 m/pixel resolution. Thus we consider a total cryolava volume of $7 \times 10^6 \text{ m}^3$. Our results presented erupted volumes ranging from 2000 to 10^8 m^3 , thus the largest eruptions considered here would be required to produce these deposits.

Larger reservoirs than these considered in this study could also be relevant for Europa, especially if they had a sheet-like shape, as observed on Earth (Sigurdsson et al., 1999). Also, cyclic eruptions might produce thicker deposits: once an initial eruption ends, remaining cryomagma in the reservoir and conduit continues to

freeze and might produce a second eruption. In this case, the final deposit, consisting of multiple superposed flows, would be thicker. To explore this further, one would need a better understanding of the heating sources and their cyclicity and a better understanding of cryomagma reservoir lifetimes.

5. Conclusions

For reservoirs located within the outermost 10 km of Europa’s ice shell, the frozen fraction of cryomagma residing in a subsurface reservoir that is required to trigger an eruption increases with reservoir depth. For pure water cryomagma, the frozen volume fraction required to trigger an eruption ranges from 2.5% to 13%, and from 4% to 26% for briny cryomagma for reservoirs located at 1 km to 10 km depth. For pure water cryomagma, the critical freezing time varies between a few days for the smallest reservoirs investigated here (i.e. 60 m radius) and 200 years for the largest ones (1300 m radius). These time-scales are an order of magnitude longer for briny cryomagma. In case of a warmer temperature gradient in the ice crust, varying from 100 to 250 K, the reservoir freezing time-scale is extended up to 1000 years for pure water and 10^4 years for a briny cryomagma. These time-scales compares to a 1-100 ky percolation time-scale (Kalousová et al., 2014), which suggests that a cryovolcanic event is thus possible before percolation of the water lens to the ocean. A comparison with the Maxwell relaxation time of the ice shows that only the reservoir at depth <5 km will always react elastically to the stress generated during freezing. For reservoirs in warmer (deeper) regions, the viscous behavior of the ice needs to be taken into account and necessitates further modeling.

The volumes erupted at the surface range from 10^3 m³ for the small reservoirs to 10^8 m³ for the largest. The eruption duration ranges from a few seconds to 20 hours for both pure water and the briny mixture used in this study. If we compare these erupted volumes with a rough estimate of the volume of cryomagma deposits of smooth deposits depicted in Fig. 15, we can infer that one eruption event occurred from the deepest (10 km) and largest (10^{10} m³) reservoirs investigated here.

In this study we show that cryovolcanic activity on Europa is not limited to large-scale features: relatively small reservoirs could erupt easily due to freezing. Detection of cryovolcanic activity at Europa’s surface might require images of higher resolution than were provided by the Galileo mission. Two upcoming missions, JUICE (ESA) and Europa Clipper (NASA), should collect high resolution images, and small cryomagmatic structures might be observed. In addition, thanks to these future missions, the ice thermal gradient and composition are expected to be better constrained. Therefore, the present work could help to link the future data concerning Europa’s surface with the geodynamical models of the interior (Sotin et al., 2002; Mitri

and Showman, 2008; Quick and Marsh, 2015) in order to better predict the feasibility of water storage and cryovolcanic activity.

Acknowledgments

We acknowledge support from the "Institut National des Sciences de l'Univers" (INSU), the "Centre National de la Recherche Scientifique" (CNRS) and "Centre National d'Etudes Spatiales" (CNES) through the "Programme National de Planétologie". We also thanks the "Institut Pierre Simon Laplace" (IPSL). We thank Anne Davaille for interesting discussions. We gratefully acknowledge Kathleen Craft and an anonymous reviewer for the very interesting comments and suggestions that permitted us to greatly improve this manuscript.

6. Appendix: Stefan's problem

In this model, we consider that at time $t = 0$, the reservoir is totally filled with liquid water, at a uniform melting temperature T_m which remains constant during the thermal transfer as it can not decrease without changing the liquid to ice. The coordinate $z = 0$ refers to the reservoir wall, whereas the coordinate $z = R$ refers to the center of the reservoir (see Fig. 3). Initially, the reservoir wall is located at position $z = 0$ and all the ice outside the reservoir (i.e. for $z < 0$) is at temperature T_{cold} . For $t > 0$, the liquid in the reservoir progressively freezes: the solidification front progresses toward the center of the reservoir. At time t , the solidification front is located at position $S(t)$, with $S(t = 0) = 0$ and $S(t \rightarrow \infty) = R$ where R is the reservoir radius.

Hereafter, the physical properties referring to the solid part of the reservoir (i.e. for $z < S(t)$) are specified with an index s , whereas the properties referring to the liquid part (i.e. for $z > S(t)$) are specified with a l index. We also delimit three different zones with their own temperature profile: T_0 in $z < 0$, T_1 in $0 < z < S$ and T_2 in $z > S$ (see Fig. 3). This permit us to take into account the thermal transfer in the ice surrounding the reservoir.

The initial and boundary conditions are summarized as follows :

$$t = 0 : \quad S(t = 0) = 0 \quad (B.C.1) \quad (27)$$

$$t > 0 : \quad T_0(z \rightarrow -\infty) = T_{cold} \quad (B.C.2)$$

$$T_0(z = 0) = T_1(z = 0) \quad (B.C.3)$$

$$T_1(z = S) = T_m \quad (B.C.4)$$

The heat transfer at the solidification front is governed by the following equation:

$$\frac{\partial T_1}{\partial t} = \kappa_s \Delta T_1 \quad (28)$$

where $\kappa_s = \frac{k_s}{\rho_s c_p}$ is the thermal diffusivity in the solid part of the reservoir, with k_s the thermal conductivity of the ice in $\text{W m}^{-1} \text{K}^{-1}$, ρ_s the pure water ice density, and c_p the pure water ice heat capacity. The thermal transfer only depends on the z coordinate, so we have, in cartesian coordinates:

$$\frac{\partial T_s}{\partial t} = \kappa_s \frac{\partial^2 T_s}{\partial z^2} \quad (29)$$

The Neumann's solution for the heat transfer takes the form (Carslaw and Jaeger, 1986):

$$\begin{aligned} T_0(z, t) &= A + B \left(1 + \text{erf} \left(\frac{z}{2\sqrt{\kappa_s t}} \right) \right) \quad (*) \\ T_1(z, t) &= C + D \text{erf} \left(\frac{z}{2\sqrt{\kappa_s t}} \right) \quad (**) \end{aligned} \quad (30)$$

(B.C.2) gives $A = T_{cold}$. (*) and (**) with (B.C.3) gives $T_{cold} + B = C$. We use the continuity in the solid medium to obtain $B = D$. Finally, with (B.C.4), we have :

$$T_0(z, t) = T_1(z, t) = T_{cold} + \frac{T_m - T_{cold}}{1 + \text{erf} \lambda} \left(1 + \text{erf} \left(\frac{z}{2\sqrt{\kappa_s t}} \right) \right) \quad (31)$$

where λ is defined as $\lambda = \frac{S}{2\sqrt{\kappa_s t}}$. Moreover, with Eq. (29) applied at $z = S$, we obtain:

$$\lambda (1 + \text{erf} \lambda) \exp \lambda^2 = \frac{(T_m - T_{cold}) c_p}{L \sqrt{\pi}} \quad (32)$$

with $\kappa_s = \frac{k_s}{\rho_s c_p}$. Numerical solution of Eq. (32) permit us to obtain λ and then to deduce the critical freezing

time τ_c required to fracture the chamber wall:

$$\tau_c = \left(\frac{S_c}{2\lambda\sqrt{\kappa_s}} \right)^2 \quad (33)$$

where S_c is the position of the solidification front at time τ_c .

References

References

- Anderson, J. D., 1998. Europa's differentiated internal structure: Inferences from four Galileo encounters. *Science* 281 (5385), 2019–2022.
- Bejan, A., 1993. *Heat Transfer*. John Wiley and Sons Ltd, 704 p.
- Bird, R. B., Stewart, W. E., Lightfoot, E. N., 1960 (First Edition). *Transport Phenomena*. John Wiley & Sons, 780 p.
- Blumm, J., Lindemann, A., 2003. Characterization of the thermophysical properties of molten polymers and liquids using the flash technique. *High Temperatures-High Pressures* 35/36 (6), 627–632.
- Carslaw, H. S., Jaeger, J. C., 1986. *Conduction of Heat in Solids* (Oxford Science Publications). Oxford University Press, 520 p.
- Craft, K. L., Patterson, G. W., Lowell, R. P., Germanovich, L., 2016. Fracturing and flow: Investigations on the formation of shallow water sills on Europa. *Icarus* 274, 297–313.
- Dalton, J. B., 2007. Linear mixture modeling of Europa's non-ice material based on cryogenic laboratory spectroscopy. *Geophysical Research Letters* 34 (21), L21205.
- Dameron, A. C., Burr, D. M., 2018. European double ridge morphometry as a test of formation models. *Icarus* 305, 225–249.
- Dombard, A. J., Patterson, G. W., Lederer, A. P., Prockter, L. M., 2013. Flanking fractures and the formation of double ridges on Europa. *Icarus* 223 (1), 74–81.
- Fagents, S. A., 2003. Considerations for effusive cryovolcanism on Europa: The post-Galileo perspective. *Journal of Geophysical Research* 108 (E12), 5139.

- Fine, R. A., Millero, F. J., 1973. Compressibility of water as a function of temperature and pressure. *The Journal of Chemical Physics* 59 (10), 5529–5536.
- Gammon, P. H., Kieft, H., Clouter, M. J., 1983. Elastic constants of ice samples by Brillouin spectroscopy. *The Journal of Physical Chemistry* 87 (21), 4025–4029.
- Greeley, R., Sullivan, R., Klemaszewski, J., Homan, K., Head, J. W., Pappalardo, R. T., Veverka, J., Clark, B. E., Johnson, T. V., Klaasen, K. P., Belton, M., Moore, J., Asphaug, E., Carr, M. H., Neukum, G., Denk, T., Chapman, C. R., Pilcher, C. B., Geissler, P. E., Greenberg, R., Tufts, R., 1998. Europa: Initial galileo geological observations. *Icarus* 135 (1), 4–24.
- Greenberg, R., Geissler, P., 2002. Europa’s dynamic icy crust. *Meteoritics & Planetary Science* 37 (12), 1685–1710.
- Greenberg, R., Hoppa, G. V., Tufts, B., Geissler, P., Riley, J., Kadel, S., 1999. Chaos on Europa. *Icarus* 141 (2), 263–286.
- Hall, D., Strobel, D., Feldman, P., McGrath, M., Weaver, H., 1995. Detection of an oxygen atmosphere on Jupiter’s moon Europa. *Nature* 373 (6516), 677.
- Hansen, G. B., 2004. Amorphous and crystalline ice on the galilean satellites: A balance between thermal and radiolytic processes. *Journal of Geophysical Research* 109 (E1).
- Harada, Y., Kurita, K., 2006. The dependence of surface tidal stress on the internal structure of Europa: The possibility of cracking of the icy shell. *Planetary and Space Science* 54 (2), 170–180.
- Head, J. W., Pappalardo, R. T., Sullivan, R., oct 1999. Europa: Morphological characteristics of ridges and triple bands from Galileo data (E4 and E6) and assessment of a linear diapirism model. *Journal of Geophysical Research: Planets* 104 (E10), 24223–24236.
- Hillier, J., Squyres, S. W., 1991. Thermal stress tectonics on the satellites of Saturn and Uranus. *Journal of Geophysical Research: Planets* 96 (E1), 15665–15674.
- Hobbs, P. V., 1975. *Ice Physics*. Oxford University Press, 856 p.
- Hogenboom, D., Kargel, J., Ganasan, J., Lee, L., 1995. Magnesium Sulfate-Water to 400 MPa using a Novel piezometer: Densities, phase equilibria, and planetological implications. *Icarus* 115 (2), 258 – 277.

- Johnston, S. A., Montési, L. G., 2014. Formation of ridges on Europa above crystallizing water bodies inside the ice shell. *Icarus* 237, 190–201.
- Kalousová, K., Souček, O., Tobie, G., Choblet, G., Čadek, O., 2014. Ice melting and downward transport of meltwater by two-phase flow in Europa's ice shell. *Journal of Geophysical Research: Planets* 119 (3), 532–549.
- Kalousová, K., Souček, O., Tobie, G., Choblet, G., Čadek, O., 2016. Water generation and transport below Europa's strike-slip faults. *Journal of Geophysical Research: Planets* 121 (12), 2444–2462.
- Kargel, J. S., 1991. Brine volcanism and the interior structures of asteroids and icy satellites. *Icarus* 94 (2), 368–390.
- Kattenhorn, S. A., Prockter, L. M., 2014. Evidence for subduction in the ice shell of Europa. *Nature Geoscience* 7 (10), 762–767.
- Khurana, K. K., Kivelson, M. G., Stevenson, D. J., Schubert, G., Russell, C. T., Walker, R. J., Polanskey, C., 1998. Induced magnetic fields as evidence for subsurface oceans in Europa and Callisto. *Nature* 395 (6704), 777–780.
- Lee, S., Pappalardo, R. T., Makris, N. C., 2005. Mechanics of tidally driven fractures in Europa's ice shell. *Icarus* 177 (2), 367–379.
- Ligier, N., Poulet, F., Carter, J., Brunetto, R., Gourgéot, F., 2016. VLT/Sinfoni observations of Europa: New insights into the surface composition. *The Astronomical Journal* 151 (6), 163.
- Lister, J. R., Kerr, R. C., 1991. Fluid-mechanical models of crack propagation and their application to magma transport in dykes. *Journal of Geophysical Research* 96 (B6), 10049.
- Litwin, K. L., Zygielbaum, B. R., Polito, P. J., Sklar, L. S., Collins, G. C., 2012. Influence of temperature, composition, and grain size on the tensile failure of water ice: Implications for erosion on Titan. *Journal of Geophysical Research* 117 (E08013).
- Manga, M., Michaut, C., 2017. Formation of lenticulae on Europa by saucer-shaped sills. *Icarus* 286, 261–269.
- Manga, M., Wang, C.-Y., 2007. Pressurized oceans and the eruption of liquid water on Europa and Enceladus. *Geophysical Research Letters* 34 (L07202).

- McCarthy, C., Cooper, R. F., Kirby, S. H., Rieck, K. D., Stern, L. A., 2007. Solidification and microstructures of binary ice-I hydrate eutectic aggregates. *American Mineralogist* 92 (10), 1550–1560.
- McLeod, P., Tait, S., 1999. The growth of dykes from magma chambers. *Journal of Volcanology and Geothermal Research* 92 (3-4), 231–245.
- Mitri, G., Showman, A. P., 2008. A model for the temperature-dependence of tidal dissipation in convective plumes on icy satellites: Implications for Europa and Enceladus. *Icarus* 195 (2), 758–764.
- Miyamoto, H., Mitri, G., Showman, A. P., Dohm, J. M., 2005. Putative ice flows on Europa: Geometric patterns and relation to topography collectively constrain material properties and effusion rates. *Icarus* 177 (2), 413–424.
- Neveu, M., Desch, S., Shock, E., Glein, C., 2015. Prerequisites for explosive cryovolcanism on dwarf planet-class Kuiper belt objects. *Icarus* 246, 48 – 64, special Issue: The Pluto System.
- Nimmo, F., 2004a. Stresses generated in cooling viscoelastic ice shells: Application to Europa. *Journal of Geophysical Research* 109 (E12001).
- Nimmo, F., 2004b. What is the Young’s modulus of ice ? In: Europa’s Icy Shell, LPI Contrib. 1195. Lunar and Planet. Inst., Houston, Tex.
- Pappalardo, R., Belton, M., Breneman, H., Carr, M., Chapman, C., Collins, G., Denk, T., Fagents, S., Geissler, P., Giese, B., et al., 1999. Does Europa have a subsurface ocean? Evaluation of the geological evidence. *Journal of Geophysical Research: Planets* 104 (E10), 24015–24055.
- Petrenko, V. F., Whitworth, R. W., 2002. *Physics of Ice*. Oxford University Press, 392 p.
- Prieto-Ballesteros, O., Kargel, J. S., 2005. Thermal state and complex geology of a heterogeneous salty crust of Jupiter's satellite, Europa. *Icarus* 173 (1), 212–221.
- Quick, L. C., Marsh, B. D., jun 2015. Constraining the thickness of Europa’s water-ice shell: Insights from tidal dissipation and conductive cooling. *Icarus* 253, 16–24.
- Quick, L. C., Marsh, B. D., 2016. Heat transfer of ascending cryomagma on Europa. *Journal of Volcanology and Geothermal Research* 319, 66–77.

- Quillen, A. C., Giannella, D., Shaw, J. G., Ebinger, C., 2016. Crustal failure on icy moons from a strong tidal encounter. *Icarus* 275, 267–280.
- Robert T. Pappalardo, William B. McKinnon, K. K., 2009. *Europa* (Space Science Series). University of Arizona Press, 720 p.
- Rubin, A. M., 1993. Tensile fracture of rock at high confining pressure: Implications for dike propagation. *Journal of Geophysical Research* 98 (B9), 15919.
- Rubin, A. M., 1995. Propagation of magma-filled cracks. *Annual Review of Earth and Planetary Sciences* 23 (1), 287–336.
- Rumble, J. R., 2002. *CRC Handbook of Chemistry and Physics*, 83rd Edition. CRC Press, 2664 p.
- Safarov, J., Millero, F., Feistel, R., Heintz, A., Hassel, E., 2009. Thermodynamic properties of standard seawater: extensions to high temperatures and pressures. *Ocean Science* 5 (3), 235–246.
- Sammis, C. G., Julian, B. R., 1987. Fracture instabilities accompanying dike intrusion. *Journal of Geophysical Research: Solid Earth* 92 (B3), 2597–2605.
- Schenk, P., Matsuyama, I., Nimmo, F., 2008. True polar wander on Europa from global-scale small-circle depressions. *Nature* 453 (7193), 368–371.
- Schmidt, B. E., Blankenship, D. D., Patterson, G. W., Schenk, P. M., 2011. Active formation of ‘chaos terrain’ over shallow subsurface water on Europa. *Nature* 479 (7374), 502–505.
- Sigurdsson, H., Houghton, B., Rymer, H., Stix, J., McNutt, S., 1999. *Encyclopedia of Volcanoes*. Academic Press, 1417 p.
- Sotin, C., Head, J. W., Tobie, G., 2002. Europa: Tidal heating of upwelling thermal plumes and the origin of lenticulae and chaos melting. *Geophysical Research Letters* 29 (8), 74–1–74–4.
- Spencer, J. R., 1999. Temperatures on europa from galileo photopolarimeter-radiometer: Nighttime thermal anomalies. *Science* 284 (5419), 1514–1516.
- Tobie, G., Choblet, G., Sotin, C., 2003. Tidally heated convection: Constraints on Europa’s ice shell thickness. *Journal of Geophysical Research: Planets* 108 (E11), 5124.

- Traversa, P., Pinel, V., Grasso, J. R., 2010. A constant influx model for dike propagation: Implications for magma reservoir dynamics. *Journal of Geophysical Research* 115 (B01201).
- Vance, S. D., Panning, M. P., Stahler, S., Cammarano, F., Bills, B. G., Tobie, G., Kamata, S., Kedar, S., Sotin, C., Pike, W. T., Lorenz, R., Huang, H.-H., Jackson, J. M., Banerdt, B., 2018. Geophysical investigations of habitability in ice-covered ocean worlds. *Journal of Geophysical Research: Planets* 123 (1), 180–205.
- Wahr, J., Selvens, Z. A., Mullen, M. E., Barr, A. C., Collins, G. C., Selvens, M. M., Pappalardo, R. T., 2009. Modeling stresses on satellites due to nonsynchronous rotation and orbital eccentricity using gravitational potential theory. *Icarus* 200 (1), 188–206.
- Zahnle, K., Schenk, P., Levison, H., Dones, L., 2003. Cratering rates in the outer solar system. *Icarus* 163 (2), 263–289.